Orbital loop currents in iron-based superconductors

Markus Klug,[1,*] Jian Kang,[2] Rafael M. Fernandes,[2] and Jörg Schmalian[1,3]

[1]*Institute for Theoretical Condensed Matter Physics, Karlsruhe Institute of Technology, D-76131 Karlsruhe, Germany*
[2]*School of Physics and Astronomy, University of Minnesota, Minneapolis, Minnesota 55455, USA*
[3]*Institute of Solid State Physics, Karlsruhe Institute of Technology, D-76344 Eggenstein-Leopoldshafen, Germany*

We show that the antiferromagnetic state commonly observed in the phase diagrams of the iron-based superconductors necessarily triggers loop currents characterized by charge transfer between different Fe $3d$ orbitals. This effect is rooted on the glide-plane symmetry of these materials and on the existence of an atomic spin-orbit coupling that couples states at the X and Y points of the 1-Fe Brillouin zone. In the particular case in which the magnetic moments are aligned parallel to the magnetic ordering vector direction, which is the moment configuration most commonly found in the iron-based superconductors, these loop currents involve the d_{xy} orbital and either the d_{yz} orbital (if the moments point along the y axis) or the d_{xz} orbitals (if the moments point along the x axis). We show that the two main manifestations of the orbital loop currents are the emergence of magnetic moments in the pnictide/chalcogen site and an orbital-selective band splitting in the magnetically ordered state, both of which could be detected experimentally. Our results highlight the unique intertwining between orbital and spin degrees of freedom in the iron-based superconductors, and reveal the emergence of an unusual correlated phase that may impact the normal state and superconducting properties of these materials.

I. INTRODUCTION

One of the hallmarks of the iron-based superconductors is the close interplay between magnetic and orbital degrees of freedom. Magnetic order is often observed in the phase diagrams of these materials, and is characterized by the ordering vectors $\mathbf{Q}_1 = (\pi,0)$ and $\mathbf{Q}_2 = (0,\pi)$ of the unfolded 1-Fe Brillouin zone [1–3]. While in most cases the magnetic ground state corresponds to spin stripes with either one of these two ordering vectors [4], several hole-doped systems display double-$\mathbf{Q}$ magnetic order consisting of a linear combination of the two possible types of order [5–8]. Orbital order is also found in the phase diagram below the nematic transition temperature, and is characterized by an unequal occupation between the Fe d_{xz} and d_{yz} orbitals, which breaks the tetragonal symmetry of the system [9–11]. At least in the iron pnictides, the evidence points to a magnetic origin of this orbital order [12], unveiling the close interaction between these two distinct degrees of freedom.

Microscopically, this interaction is described by the atomic spin-orbit coupling (SOC), given by the term $\lambda \mathbf{S} \cdot \mathbf{L}$. ARPES measurements have established that the magnitude of the SOC λ ranges from around 10 meV in the 122-compounds up to 25 meV in the 11-compounds [13]. Such an energy scale is comparable to the band splitting caused by orbital order, to the superconducting gap, and to the spin-density wave gap. Therefore, the SOC is an integral and necessary ingredient in the description of the low-energy properties of the iron-based superconductors [14]. Besides the coupling between spin-driven nematicity and orbital order discussed above, SOC

also selects the magnetic moment direction in the stripe phase to be generally parallel to the ordering vector [15,16].

In this work, we demonstrate another important consequence of the SOC, which has hitherto been unexplored. In particular, we show that long-range spin order necessarily generates loop currents in which charge is transferred between Fe orbitals at different sites, hence the name orbital loop currents. Although in this paper we focus on the case of stripe spin magnetic order, the effect is general and should be present even in double-$\mathbf{Q}$ magnetically ordered states, as well as independent of the specific microscopic mechanism for magnetism, e.g., itinerant or localized magnetic moments, since it is solely based on symmetry. The qualitative argument for this effect is general, and can be outlined as follows. To keep the notation simple, let us introduce the intraorbital stripe magnetic order parameter m with ordering vector $\mathbf{Q}_i$ and the interorbital imaginary charge-density wave ϕ with ordering vector $\mathbf{Q}_j$. Note that both orders break translational and tetragonal symmetries, as well as time-reversal symmetry. Because the latter is broken in spin space by m and in real space by ϕ, only SOC can couple both order parameters. In terms of a general Ginzburg-Landau free-energy expansion, one expects the following bilinear coupling:

$$\delta F = g(\lambda)\phi\, m, \tag{1}$$

where the coupling constant $g(\lambda)$ depends on the strength of SOC λ such that $g(\lambda = 0) = 0$. At first sight, one may think that this coupling is only allowed if $\mathbf{Q}_j = \mathbf{Q}_i$ due to momentum conservation. However, a key property of the iron-based superconductors is the glide-plane symmetry of the FeAs plane [17–20], which doubles the size of the unit cell to one containing 2 Fe atoms, making $\mathbf{Q}_1$ and $\mathbf{Q}_2$ equivalent in the actual crystallographic unit cell. Thus, depending on the

orbital composition of ϕ, magnetic order with ordering vector $\mathbf{Q}_1$ will trigger imaginary charge-density wave with ordering vector $\mathbf{Q}_2$. An alternative way to interpret this coupling is to note that the SOC λ that couples states at the X and Y points of the 1-Fe Brillouin zone [14,15] provide the momentum transfer $\mathbf{Q}_1 + \mathbf{Q}_2$ required by such a coupling.

An interorbital imaginary charge-density wave corresponds to charge currents in real space. The interorbital character of this order implies that charge is transferred between different orbitals at different sites. Charge conservation, however, requires these charge currents to form closed loops. Thus, hereafter we refer to this type of order as an orbital loop-current order. Note that the loop currents discussed here break the translational symmetry of the lattice by changing sign between neighboring Fe lattice sites; as a result, they are compatible with Bloch's theorem, which prohibits a static current carrying ground state [21,22].

Interestingly, a similar type of loop-current order, defined in band basis instead of orbital basis, was introduced by Ref. [23] to explain the tetragonal symmetry breaking of the iron-based superconductors. Reference [24] proposed the existence of an imaginary charge-density wave based on an enhanced symmetry associated with nested Fermi pockets. In Ref. [25], the combined effects of loop-current fluctuations and magnetic fluctuations was proposed to enhance the nematic transition temperature of materials with very small Fermi energies, such as FeSe. Whether the loop-current order can spontaneously order as a primary order, rather than a secondary order triggered by magnetic order, remains an open question that is only sharply defined for small λ anyway. Renormalization group calculations, performed in the band basis, suggest that on-site repulsive interactions generally select magnetic order over loop-current order [26]. We also note that loop-current order has also been investigated in cuprate superconductors, either as a $\mathbf{Q} = 0$ intra-unit-cell order involving the Cu and the O orbitals [27], or as a translational symmetry-breaking order also known as d-density wave [28]. Note that, in our case, the loop-current order is necessarily accompanied by magnetic order, and it also breaks the tetragonal symmetry of the lattice.

In the remainder of the paper, we derive the results outlined above from a low-energy microscopic model for the iron-based superconductors that respect all the crystal symmetries of the FeAs plane, including the glide plane symmetry [15,17]. This low-energy model relies on the smallness of the Fermi energy of these materials to perform a $\mathbf{k} \cdot \mathbf{p}$ expansion near high-symmetry points of the lattice. As a result, only three Fe orbitals are taken into account, namely the xz, yz, and the xy 3d orbitals, since these orbitals are responsible for the band dispersions in the vicinity of the Fermi surface. Additional electronic degrees of freedom, such as electronic states located at the pnictogen/chalcogen lattice sites, or the two remaining Fe 3d orbitals, are assumed to be integrated out, thus renormalizing the model's parameters. We stress that our main results are general and independent of the particular choice of parameters.

Using this model, we derive the different orbital loop-current configurations that are allowed by symmetry and triggered by the three different types of long-range magnetic stripe order, providing explicit expressions for the coupling constant $g(\lambda)$ introduced in Eq. (1) above. For the most experimentally

relevant case of stripe order with magnetic moments pointing parallel to the wave vectors $\mathbf{Q}_1$ and $\mathbf{Q}_2$, we find that the loop currents involve d_{xy}/d_{yz} and d_{xy}/d_{xz} orbitals, respectively. We also discuss two manifestations of these orbital loop-current orders, which can be detected experimentally. The first one is the magnetization profile induced by the loop currents that follows from simple electrodynamic considerations. The main result is the appearance of magnetic moments on the pnictide/chalcogen sites pointing out of the plane, in contrast to the magnetic moments on the Fe sites, which point in the plane. The second manifestation that we discuss is the spectroscopic signature of the orbital loop-current order parameter on the electronic spectrum. In the particular case in which the spins in the magnetic stripe state point in the plane, we show that the magnetic order parameter M and the orbital loop-current order parameter ϕ contribute to splittings of different doublets at the corner of the 2-Fe Brillouin zone. Consequently, we propose to use ARPES to assess the impact of orbital loop-current order on the normal-state electronic spectrum of the pnictides.

The paper is organized as follows. Section II introduces the microscopic model, whereas Sec. III classifies the different types of orbital loop current allowed by the different types of stipe magnetic order. Section IV derives the microscopic coupling between these two types of order, mediated by the SOC, while Sec. V presents the experimental manifestations of orbital loop-current order. Conclusions are presented in Sec. VI. To help the reader navigate the paper, Appendix A describes the various quantities defined throughout the main text. Appendix B shows the explicit form of the band dispersions, whereas Appendix C presents explicit expressions for the vertex functions needed in the diagrammatic calculations.

II. MICROSCOPIC LOW-ENERGY MODEL

Instead of the full electronic model, which requires 10 Fe orbitals per unit cell (5 per Fe site), we consider a reduced orbital-projected band model. This electronic model was derived previously by employing the symmetry properties of the underlying crystal structure [15] and by expanding the tight-binding dispersion of the electronic states around the high symmetry points of the Brillouin zone [16]. It therefore represents an effective low-energy model of electronic states in the vicinity of the Fermi surfaces located at these high symmetry points. Electronic states residing on pnictogen/chalcogenide lattice sites are energetically well below or above the Fermi surface and are therefore assumed to effectively renormalize the model's parameters. Besides its simplicity, the full symmetry properties of the nonsymmorphic $P4/nmm$ space group characterizing a single Fe-pnictogen/chalcogen plane are encoded in this model, including the glide-plane symmetry resulting from the alternate stacking of the pnictogen/chalcogen atoms. For the sake of brevity, we review here only the aspects of this model necessary for our analysis. A more detailed derivation of this model can be found in Refs. [15,16] or in the review [17].

Before presenting the model, we first comment on the representation of the electronic states in the 2-Fe and 1-Fe unit cells to clarify the notation. As discussed above, the 2-Fe unit cell represents the actual crystallographic unit cell, with the corresponding 2-Fe Brillouin zone described in terms of the real crystal momenta of the electronic states following Bloch's

theorem. Alternatively, the electronic states can be represented in the 1-Fe unit cell in terms of the spatial coordinates x and y connecting nearest-neighbor Fe lattice sites, as well as in the corresponding 1-Fe Brillouin zone described in terms of pseudocrystal momenta k_x and k_y [19,29]. For the sake of simplicity, we will express all states in the 1-Fe Brillouin zone notation, highlighting the difference between real and pseudocrystal momentum if necessary.

The low-energy electronic model consists of two holelike Fermi pockets located at the $\Gamma = (0,0)$ point of the 1-Fe Brillouin zone and two electronlike Fermi pockets located at $X = (\pi,0)$ and $Y = (0,\pi)$. Electronic states around Γ transform as the irreducible E_g representation of the tetragonal D_{4h} point group [15], forming therefore an orbital doublet composed of degenerate xz and yz Fe orbitals (oriented along the Fe-Fe direction). Thus, it is convenient to introduce the doublet

$$\psi_{\Gamma,\mathbf{k}\sigma} = \begin{pmatrix} d_{yz,\mathbf{k}\sigma} \\ -d_{xz,\mathbf{k}\sigma} \end{pmatrix}. \qquad (2)$$

Electronic states near the X and Y points form two electron pockets centered at momenta $\mathbf{Q}_1 = (\pi,0)$ and $\mathbf{Q}_2 = (0,\pi)$, composed of yz/xy and xz/xy orbitals, respectively. Thus, we introduce two additional doublets:

$$\psi_{X,\mathbf{k}+\mathbf{Q}_1\sigma} = \begin{pmatrix} d_{yz,\mathbf{k}+\mathbf{Q}_1\sigma} \\ d_{xy,\mathbf{k}+\mathbf{Q}_1\sigma} \end{pmatrix} \quad \text{and} \qquad (3a)$$

$$\psi_{Y,\mathbf{k}+\mathbf{Q}_2\sigma} = \begin{pmatrix} d_{xz,\mathbf{k}+\mathbf{Q}_2\sigma} \\ d_{xy,\mathbf{k}+\mathbf{Q}_2\sigma} \end{pmatrix}. \qquad (3b)$$

Because of the glide-plane symmetry of the system, which makes the system invariant under a $(\frac{1}{2},\frac{1}{2})$ lattice translation (in the 2-Fe unit cell) followed by a mirror reflection with respect to the plane, the elements of the two doublets transform according to the two-dimensional irreducible representations (denoted E_{Mi}) of the $P4/nmm$ group at the $M = (\pi,\pi)$ point of the 2-Fe Brillouin zone. In particular, the upper components form another doublet that transforms as E_{M1} whereas the lower components form a doublet that transforms as E_{M3}.

The effective tight-binding Hamiltonian in real space is then given by

$$H_0 = \sum_{ij\sigma} t_{ij}^{a,b} (d_{a,i\sigma}^\dagger d_{b,j\sigma} + \text{H.c.}) \qquad (4)$$

with hopping amplitude $t_{ij}^{a,b}$ representing the wave function's overlap of orbitals a and b at Fe lattice site i and j. Represented in reciprocal space, the Hamiltonian is given by

$$\begin{aligned} H_0 = &\sum_{\mathbf{k}\sigma} \psi_{\Gamma,\mathbf{k}\sigma}^\dagger \epsilon_{\mathbf{k}}^\Gamma \psi_{\Gamma,\mathbf{k}\sigma} \\ &+ \sum_{\mathbf{k}\sigma} \psi_{X,\mathbf{k}+\mathbf{Q}_1\sigma}^\dagger \epsilon_{\mathbf{k}}^X \psi_{X,\mathbf{k}+\mathbf{Q}_1\sigma} \\ &+ \sum_{\mathbf{k}\sigma} \psi_{Y,\mathbf{k}+\mathbf{Q}_2\sigma}^\dagger \epsilon_{\mathbf{k}}^Y \psi_{Y,\mathbf{k}+\mathbf{Q}_2\sigma}, \end{aligned} \qquad (5)$$

where ϵ^Γ, ϵ^X, and ϵ^Y are 2×2 matrices acting in the orbital doublet space, whose explicit expressions are given in Appendix C. Diagonalizing these matrices gives the corresponding band dispersions of the electronic states.

The atomic spin-orbit coupling, $H_{\text{SOC}} = \lambda \mathbf{S} \cdot \mathbf{L}$, gives an additional contribution to the noninteracting Hamiltonian [15,16]:

$$\begin{aligned} H_{\text{SOC}} = &i\frac{\lambda}{2} \sum_{\mathbf{k}\alpha\beta} (d_{xz,\mathbf{k}\alpha}^\dagger \sigma_{\alpha\beta}^z d_{yz,\mathbf{k}\beta} - \text{H.c.}) \\ &+ i\frac{\lambda}{2} \sum_{\mathbf{k}\alpha\beta} (d_{xz,\mathbf{k}+\mathbf{Q}_2\alpha}^\dagger \sigma_{\alpha\beta}^x d_{xy,\mathbf{k}+\mathbf{Q}_1\beta} - \text{H.c.}) \\ &+ i\frac{\lambda}{2} \sum_{\mathbf{k}\alpha\beta} (d_{yz,\mathbf{k}+\mathbf{Q}_1\alpha}^\dagger \sigma_{\alpha\beta}^y d_{xy,\mathbf{k}+\mathbf{Q}_2\beta} - \text{H.c.}) \quad (6) \end{aligned}$$

with Pauli matrix σ^a acting on spin space. The first term shows that, at the center of the Brillouin zone, SOC mixes the xz and yz orbitals, lifting the degeneracy of the orbital doublet. The second term, on the other hand, couples the electronic states located at the X and Y points. This term does not violate momentum conservation because the xy orbital has real crystal momentum $\mathbf{k} + \mathbf{Q}_i + (\pi,\pi) = \mathbf{k} + \mathbf{Q}_{\bar{i}}$ (with $\bar{1} = 2$ and $\bar{2} = 1$) due to the glide-plane symmetry affecting differently even and odd orbitals [29]. In terms of the doublets introduced above, the SOC Hamiltonian is given by:

$$\begin{aligned} H_{\text{SOC}} = &\sum_{\mathbf{k}\sigma} \psi_{\Gamma,\mathbf{k}\alpha}^\dagger \Lambda_{\Gamma,\alpha\beta}^{\text{SOC}} \psi_{\Gamma,\mathbf{k}\beta} \\ &+ \sum_{\mathbf{k}} (\psi_{X,\mathbf{k}+\mathbf{Q}_1\alpha}^\dagger \Lambda_{M,\alpha\beta}^{\text{SOC}} \psi_{Y,\mathbf{k}+\mathbf{Q}_2\beta} + \text{H.c.}) \quad (7) \end{aligned}$$

with the vertices:

$$\Lambda_\Gamma^{\text{SOC}} = i\frac{\lambda}{2} \begin{pmatrix} 0 & -1 \\ 1 & 0 \end{pmatrix} \sigma^z, \qquad (8a)$$

$$\Lambda_M^{\text{SOC}} = i\frac{\lambda}{2} \left[\begin{pmatrix} 0 & 1 \\ 0 & 0 \end{pmatrix} \sigma^x + \begin{pmatrix} 0 & 0 \\ 1 & 0 \end{pmatrix} \sigma^y \right]. \qquad (8b)$$

III. CLASSIFICATION OF MAGNETIC AND ORBITAL LOOP-CURRENT ORDERS

Having established the microscopic model, we now classify the possible types of stripe spin-density wave (SDW) order and orbital loop-current (OLC) order allowed by the symmetries of the system.

A. Magnetic order

The SDW order realized in the iron pnictides is parametrized in terms of magnetic order parameters $\mathbf{m}_{\mathbf{Q}_j}$ associated with each of the two magnetic ordering vectors $\mathbf{Q}_1 = (\pi,0)$ and $\mathbf{Q}_2 = (0,\pi)$. Generally, these order parameters are 2×2 tensors in orbital space and vectors in spin space. They are defined in terms of the electronic operators according to (summation over spin indices is left implicit):

$$\mathbf{m}_{\mathbf{Q}_j}^{(a,b)} \propto \sum_{\mathbf{k}} \langle d_{a,\mathbf{k}\alpha}^\dagger \boldsymbol{\sigma}_{\alpha\beta} d_{b,\mathbf{k}+\mathbf{Q}_j\beta} + \text{H.c.} \rangle \qquad (9)$$

with α,β corresponding to spin indices and a,b to orbital indices. Thus, we can write down the SDW Hamiltonian:

$$H_{\text{SDW}} = \sum_{\mathbf{k}j,ab} \mathbf{m}_{\mathbf{Q}_j}^{(a,b)} \cdot (d_{a,\mathbf{k}\alpha}^\dagger \boldsymbol{\sigma}_{\alpha\beta} d_{b,\mathbf{k}+\mathbf{Q}_j\beta} + \text{H.c.}). \qquad (10)$$

TABLE I. Possible intraorbital spin density-wave and orbital loop-current orders, classified by the two-dimensional irreducible representations $E_{Mi} : (E_{Mi}^+, E_{Mi}^-)$ of the $P4/nmm$ space group [15]. Also represented in the table are the spin composition and orbital composition of each order, corresponding to the indices a and b defined in Eqs. (9) and (13). In the case of SDW order, the orbital composition is intraorbital $a = b$. In the case of orbital loop-current order, the spin composition is trivial. Due to the trivial transformation behavior of the free energy, there is only a bilinear coupling between spin magnetic and loop-current orders that share the same symmetry properties, i.e., that transform according to the same irreducible representations. Here, fields listed in the same line can couple bilinearly in the free-energy expansion.

irrep of $P4/nmm$ space group	intraorbital spin order		orbital loop current order	
	field	orbital and spin comp.	field	orbital composition
$\begin{pmatrix} E_{M1}^+ \\ E_{M1}^- \end{pmatrix}$	$\begin{pmatrix} m_{\mathbf{Q}_2}^y \\ m_{\mathbf{Q}_1}^x \end{pmatrix}$	$\begin{pmatrix} xz, \sigma^y \\ yz, \sigma^x \end{pmatrix}$	$\begin{pmatrix} \phi_{\mathbf{Q}_1}^{(yz,xy)} \\ \phi_{\mathbf{Q}_2}^{(xz,xy)} \end{pmatrix}$	$\begin{pmatrix} yz, xy \\ xz, xy \end{pmatrix}$
$\begin{pmatrix} E_{M2}^+ \\ E_{M2}^- \end{pmatrix}$	$\begin{pmatrix} m_{\mathbf{Q}_2}^x \\ m_{\mathbf{Q}_1}^y \end{pmatrix}$	$\begin{pmatrix} xz, \sigma^x \\ yz, \sigma^y \end{pmatrix}$	$\begin{pmatrix} \phi_{\mathbf{Q}_1}^{(xz,xy)} \\ \phi_{\mathbf{Q}_2}^{(yz,xy)} \end{pmatrix}$	$\begin{pmatrix} xz, xy \\ yz, xy \end{pmatrix}$
$\begin{pmatrix} E_{M3}^+ \\ E_{M3}^- \end{pmatrix}$	$\begin{pmatrix} m_{\mathbf{Q}_1}^z \\ m_{\mathbf{Q}_2}^z \end{pmatrix}$	$\begin{pmatrix} yz, \sigma^z \\ xz, \sigma^z \end{pmatrix}$	$\begin{pmatrix} \phi_{\mathbf{Q}_1}^{(xz,yz)} \\ \phi_{\mathbf{Q}_2}^{(yz,xz)} \end{pmatrix}$	$\begin{pmatrix} xz, yz \\ yz, xz \end{pmatrix}$
$\begin{pmatrix} E_{M4}^+ \\ E_{M4}^- \end{pmatrix}$	$-$	$-$	$\begin{pmatrix} \phi_{\mathbf{Q}_1}^{(yz,yz)} \\ \phi_{\mathbf{Q}_2}^{(xz,xz)} \end{pmatrix}$	$\begin{pmatrix} yz, yz \\ xz, xz \end{pmatrix}$

Hereafter, we focus on intraorbital SDW, $a = b$, which is believed to be the leading magnetic instability in the iron-based superconductors [16,30]. Now, SDW order involves combinations of electronic states at the Γ and X/Y points of the 1-Fe Brillouin zone. Because in our low-energy model the electronic states at Γ contain only contributions from xz/yz orbitals, whereas the states at X have contributions from yz/xy and at Y, from xz/xy, there is only one intraorbital component $\mathbf{m}_{\mathbf{Q}_j}^{(a,a)}$ relevant for each ordering vector $\mathbf{Q}_j$, namely, $a = yz$ for $\mathbf{Q}_1 = (\pi, 0)$ and $a = xz$ for $\mathbf{Q}_2 = (0, \pi)$. Therefore, to simplify the notation, hereafter we set:

$$\mathbf{m}_{\mathbf{Q}_1} \equiv \mathbf{m}_{\mathbf{Q}_1}^{(yz,yz)} \quad \mathbf{m}_{\mathbf{Q}_2} \equiv \mathbf{m}_{\mathbf{Q}_2}^{(xz,xz)}. \quad (11)$$

Note that, since only the xz and yz orbitals are involved, the pseudocrystal momentum for the SDW order parameters coincides with the real crystal momentum. In the case of stripe SDW, which is our interest here, it follows that either $\mathbf{m}_{\mathbf{Q}_1} = 0$ or $\mathbf{m}_{\mathbf{Q}_2} = 0$.

As pointed out in Ref. [15], the possible long-range magnetic orders are classified by the irreducible representations of the $P4/nmm$ space group at the M point of the 2-Fe Brillouin zone. In particular, the six different vector components of the two $\mathbf{m}_{\mathbf{Q}_j}$ order parameters are grouped in three doublets, which transform according to the three two-dimensional irreducible representations E_{Mi} with $i \in \{1, 2, 3\}$. The full classification is presented in Table I. Note that with the constraint of intraorbital order only, there is no magnetic order that transforms as the irreducible representation E_{M4}.

Thus, this classification allows us to write the SDW order parameters not as two three-dimensional vector order parameters $m_{\mathbf{Q}_j}^\alpha$ (with $\alpha = x, y, z$ and $j = 1, 2$), but rather as three doublets $M_{E_{M_i}}^\mu$, with $i \in \{1, 2, 3\}$ denoting the appropriate irreducible representation, and $\mu \in \{+, -\}$ denoting the component of the doublet. The relationship between these two representations are those already presented in Table I. In what follows, we will use the $M_{E_{Mi}}^\mu$ notation for convenience. Their physical interpretation is straightforward: the doublet component μ corresponds to either $\mathbf{Q}_1$ or $\mathbf{Q}_2$ order. Moreover, $M_{E_{M1}}^\mu$ corresponds to stripes with in-plane moments parallel to $\mathbf{Q}_j$, i.e., the one frequently observed in iron-based systems; $M_{E_{M2}}^\mu$ corresponds to stripes with in-plane moments perpendicular to $\mathbf{Q}_j$; and $M_{E_{M3}}^\mu$ corresponds to stripes with out-of-plane moments.

In our weak-coupling approach, magnetism arises from low-energy states near the Fermi level. In some iron-based systems, there is also another hole pocket made out of d_{xy} orbitals centered at the point $M = (\pi, \pi)$ of the 1-Fe Brillouin zone (equivalent to the Γ point of the 2-Fe Brillouin zone). As a result, it is possible to form intraorbital magnetic order parameters in Eq. (9) with $a = b = xy$. These xy SDW order parameters are classified in identical manner as the ones involving the xz and yz orbitals, via the two-dimensional irreducible representations $E_{Mi} : (E_{Mi}^+, E_{Mi}^-)$ of the $P4/nmm$ space group. This classification is presented in the Appendix in Table VIII. Clearly, by symmetry, the same types of OLC order are induced by $(\pi, 0)$ or $(0, \pi)$ magnetic order parameters, regardless of their orbital composition. Thus, while in the remainder of the paper we will focus for simplicity on the microscopic model that does not have intraorbital xy magnetism, the qualitative results remain the same even if one includes this type of SDW order parameters.

B. Orbital loop-current order

To classify the different types of translational symmetry-breaking orbital loop-current (OLC) order, we look for bilinear combinations of fermionic field operators with momentum transfer $\mathbf{Q}_1$ and $\mathbf{Q}_2$ that are trivial in spin space while breaking time-reversal symmetry. Therefore, in analogy to the SDW order parameters, the most general OLC order parameter is given in terms of the orbital electronic operators by:

$$\phi_{\mathbf{Q}_j}^{(a,b)} \propto \sum_{\mathbf{k}} i \langle d_{a,\mathbf{k}\sigma}^\dagger d_{b,\mathbf{k}+\mathbf{Q}_j\sigma} - \text{H.c.} \rangle \quad (12)$$

yielding the following OLC Hamiltonian:

$$H_{\text{OLC}} = \sum_{\mathbf{k} j, ab} i \, \phi_{\mathbf{Q}_j}^{(a,b)} (d_{a,\mathbf{k}\sigma}^\dagger d_{b,\mathbf{k}+\mathbf{Q}_j\sigma} - \text{H.c.}). \quad (13)$$

Similarly to the case of the SDW orders, the different types of OLC orders must transform according to one of the three two-dimensional irreducible representations E_{M_i}. Consequently, this restricts the possible orbital indices $\phi_{\mathbf{Q}_j}^{(a,b)}$. The orbital composition of all possible orbital loop-current orders and their classification in terms of the E_{M_i} irreducible representation of the $P4/nmm$ space group is given in Table I. In analogy to the notation introduced in the SDW case, we will express the OLC order parameters also in terms of their corresponding doublets, denoted by $\Phi_{E_{M_i}}^\mu$.

TABLE II. Leading-order hopping processes between Fe lattice sites [31] that are used to construct the loop-current patterns depicted in Fig. 1. NN and NNN refer to nearest- and next-nearest-neighbor hopping, respectively.

coupled Fe orbitals	leading order hopping processes
xz and xy	NN along x
yz and xy	NN along y
xz and yz	NNN along $x \pm y$

Note that, in contrast to the SDW orders, we can construct a loop-current order, which transforms as the irreducible representation E_{M4}. This is the only type of OLC order that is intraorbital; all other ones are interorbital order. Because this OLC order cannot couple to any intraorbital SDW order, this component will not be considered hereafter. We also point out that the two orbital loop-current orders that couple xz/yz orbitals with xy orbitals (corresponding to the E_{M1} and E_{M2} irreducible representations) actually carry real crystal momentum $\mathbf{Q}_{\mathrm{Real}} = \mathbf{Q}_i + (\pi,\pi) = \mathbf{Q}_{\bar{i}}$. Thus, these OLC order parameters $\phi_{\mathbf{Q}_i}$ must couple to an SDW order parameter with momentum $\mathbf{Q}_{\bar{i}}$, instead of momentum $\mathbf{Q}_i$, as one would naively expect. The difference in pseudocrystal momentum is compensated by the out-of-plane position of the pnictogen/chalcogenide lattice sites as we will see later in the discussion of loop-current-induced magnetic moments in Sec. V.

Due to charge conservation, the OLC orders are represented in real space by closed current loops. The link between the order parameter $\phi_{\mathbf{Q}_j}^{(a,b)}$ and the physical electronic currents is established by considering the current operator $\hat{\mathbf{j}}_{ij}$ between lattice sites i and j with distance $\mathbf{R}_{ij} \equiv \mathbf{R}_i - \mathbf{R}_j$:

$$\hat{\mathbf{j}}_{ij} = \sum_{ab} \hat{\mathbf{j}}_{ij}^{ab} = \frac{ie}{\hbar} \frac{\mathbf{R}_{ij}}{R_{ij}} \sum_{ab\sigma} t_{ij}^{a,b}(d_{j,a\sigma}^{\dagger} d_{i,b\sigma} - \mathrm{H.c.}), \quad (14)$$

where $t_{ij}^{a,b}$ refers to the hopping amplitudes introduced in context of the tight-binding Hamiltonian Eq. (4), corresponding to the overlap of localized Wannier states.

The key point is that a nonvanishing OLC order parameter causes a finite expectation value for the current operator. Consequently, the resulting loop-current patterns depend on the hopping matrix elements $t_{ij}^{a,b}$. Depending on the amplitude of the different elements $t_{ij}^{a,b}$ connecting different sites i and j and orbitals a and b, arbitrary complex current patterns can be constructed in principle. However, the symmetry properties of the resulting current pattern do not depend on the actual set and strength of possible hopping processes. For the sake of simplicity, we therefore consider the leading-order hopping parameters involving either nearest- or next-nearest neighbors for each combination of orbitals, as summarized in Table II. To construct the appropriate loop-current patterns for each orbital loop-current order parameter $\phi_{\mathbf{Q}_j}^{(a,b)}$, we take into account the corresponding hopping parameters of Table II, combined with the additional constraint for local charge conservation

$$\sum_j |\langle \hat{\mathbf{j}}_{ij} \rangle| = 0, \quad \forall i. \quad (15)$$

As an example, let us show explicitly how to obtain the loop-current pattern corresponding to $\phi_{\mathbf{Q}_2}^{(xz,xy)}$ (E_{M1}^{-} irreducible representation). The dominating hopping process connecting xz and xy orbitals is the nearest-neighbor hopping along the x direction [31]. Thus, the dominating contribution to the current is given by:

$$\langle \hat{\mathbf{j}} \rangle_{ij'}^{xz,xy} = \frac{ie}{\hbar} \hat{\mathbf{e}}_x t_{ij'}^{xz,xy} \langle d_{j',xz\sigma}^{\dagger} d_{i,xy\sigma} - \mathrm{H.c.} \rangle \quad (16)$$

for all nearest neighbors j', which fulfill $\mathbf{R}_{j'} = \mathbf{R}_i \pm \hat{\mathbf{e}}_x$. Here, $\hat{\mathbf{e}}_x$ represents the unit vector along the x direction. Taking the Fourier transform, we find:

$$\langle \hat{\mathbf{j}} \rangle_{ij'}^{xz,xy} = \frac{ie}{\hbar} \hat{\mathbf{e}}_x t_{ij'}^{xz,xy} \sum_{\mathbf{k},\mathbf{p}} e^{-i(\mathbf{k}-\mathbf{p})\cdot\mathbf{R}_i} e^{-i\mathbf{k}\cdot\hat{\mathbf{e}}_x}$$
$$\times \langle d_{\mathbf{k},xz\sigma}^{\dagger} d_{\mathbf{p},xy\sigma} - \mathrm{H.c.} \rangle. \quad (17)$$

In the case of $\phi_{\mathbf{Q}_2}^{(xz,xy)}$ order, only $\mathbf{p} = \mathbf{k} + \mathbf{Q}_2$ survives in the sum above, yielding:

$$\langle \hat{\mathbf{j}} \rangle_{ij'}^{xz,xy} \propto \frac{e}{\hbar} \hat{\mathbf{e}}_x t_{ij'}^{xz,xy} \phi_{\mathbf{Q}_2}^{xz,xy} e^{i\mathbf{Q}_2\cdot\mathbf{R}_i}, \quad (18)$$

where, in the last step, we used the fact that $e^{-i\mathbf{k}\cdot\hat{\mathbf{e}}_x} \approx 1$ since the magnitude of $\mathbf{k}$ is restricted to small values. Thus, there is a constant flow along the x direction, which changes sign as one changes the spatial position along the y direction due to the oscillating factor $e^{i\mathbf{Q}_2\cdot\mathbf{R}_i}$, thus preserving local charge conservation as demanded.

The analysis for other types of loop-current orders works analogously, resulting in the loop-current patterns for $\phi_{\mathbf{Q}_2}^{(xz,xy)}$, $\phi_{\mathbf{Q}_2}^{(yz,xy)}$, and $\phi_{\mathbf{Q}_1}^{(xz,yz)}$ depicted in Fig. 1, where we assume periodic boundary conditions. As explained above, the current patterns displayed are one contribution to the total current flow present. However, they posses the full symmetry properties imposed by their classification into the three irreducible representations, providing thus insight onto the relationship between the OLC order parameters to microscopic charge flows. Moreover, we emphasize that the intersite flow between the Fe lattice sites is actually mediated by the pnictogen/chalcogen lattice sites, though their electronic degrees of freedom are integrated out in our microscopic model. This will be relevant to discuss the experimental manifestations on OLC orders below.

IV. MICROSCOPIC COUPLING BETWEEN MAGNETIC AND ORBITAL LOOP-CURRENT ORDERS

The analysis of the previous section reveals a set of three magnetic order parameters $M_{E_{Mi}}^{\mu}$ and three orbital loop-current order parameters $\Phi_{E_{Mi}}^{\mu}$ that transform according to the same two-dimensional irreducible representations E_{Mi}, with $i = 1, 2, 3$ and $\mu \in \{+,-\}$ denoting the two elements of each doublet. As a result, symmetry dictates that if $M_{E_{Mi}}^{\mu} \neq 0$, the corresponding $\Phi_{E_{Mi}}^{\mu}$ must also become nonzero. In other words, stripe SDW order induces OLC in the iron-based superconductors. Mathematically, this implies that the Ginzburg-Landau free-energy expansion of this model must contain bilinear terms of the form $g_{E_{Mi}}^{\mu} M_{E_{Mi}}^{\mu} \Phi_{E_{Mi}}^{\mu}$. In this section, we derive microscopically these coupling constants $g_{E_{Mi}}^{\mu}$. Since Φ transforms trivially in spin space, it is clear that the coupling

○ Fe, ⊕ As sites ● xz–orbitals ● xy–orbitals

(a)

○ Fe, ⊕ As sites ● yz–orbitals ● xy–orbitals

(b)
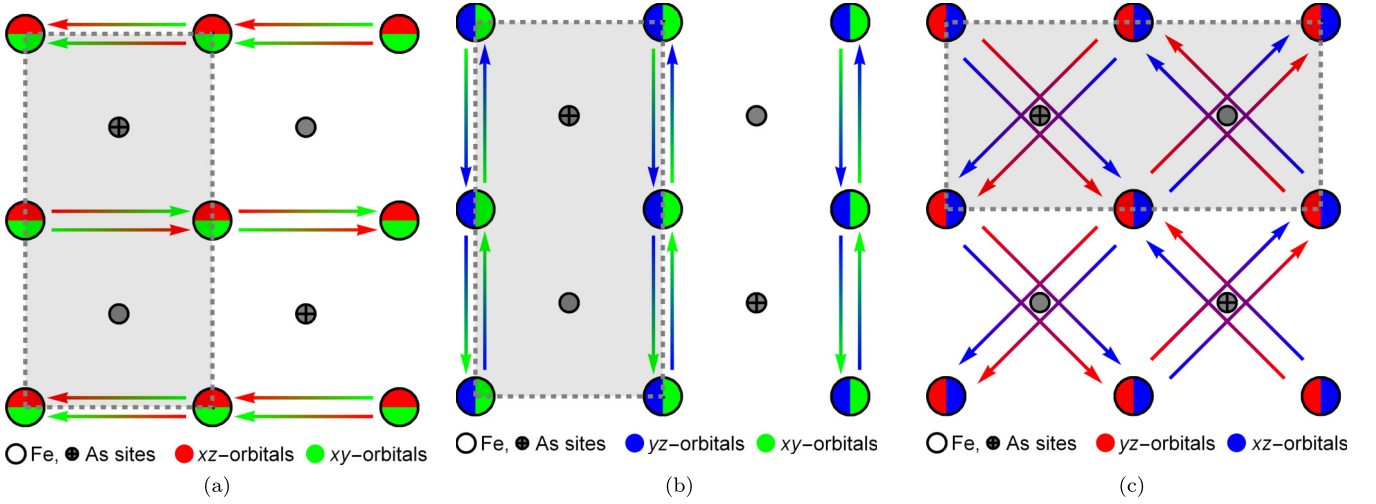
○ Fe, ⊕ As sites ● yz–orbitals ● xz–orbitals

(c)

FIG. 1. Loop-current patterns of three different OLC ground states, one for each possible irreducible representation E_{Mi}^{μ} where periodic boundary conditions are assumed. The representation of the μ component not depicted in each panel is obtained by performing a mirror reflection with respect to planes whose normals are along the diagonals of the 1-Fe unit cell. To create these configurations, only leading order Fe-Fe hopping parameters are considered. The coloring of the arrows representing the electronic flows refers to their orbital composition. Small gray circles refer to pnictogen/chalcogen sites lying above (crossed circles) or below (noncrossed circles) the Fe plane; the large circles represent Fe lattice sites. Shaded rectangles indicate the enlarged unit cell due to the translational symmetry breaking imposed by the OLC order. (a) Loop current order belonging to the irrep E_{M1}^{-} : $\phi_{Q_2}^{(xz,xy)}$, (b) Loop current order belonging to the irrep E_{M2}^{-} : $\phi_{Q_2}^{(yz,xy)}$, and (c) Loop current order belonging to the irrep E_{M3}^{+} : $\phi_{Q_1}^{(xz,yz)}$.

constants must be nonzero only in the presence of the SOC, i.e., $g_{E_{Mi}}^{\mu}(\lambda = 0) = 0$.

The free-energy functional is obtained by following the standard procedure of integrating out the electronic degrees of freedom [32]. The noninteracting Hamiltonian was already defined in Sec. II. Introducing the 12-dimensional enlarged electronic spinor $\Psi_{\mathbf{k}} = (\psi_{\Gamma,\mathbf{k}}, \psi_{X,\mathbf{k}+\mathbf{Q}_1}, \psi_{Y,\mathbf{k}+\mathbf{Q}_2})^{\mathrm{T}}$ associated with the low-energy electronic states, we can write it in the compact form:

$$H_0 = \sum_{\mathbf{k}} \Psi_{\mathbf{k}}^{\dagger} \mathcal{H}_0 \Psi_{\mathbf{k}} \quad H_{\mathrm{SOC}} = \sum_{\mathbf{k}} \Psi_{\mathbf{k}}^{\dagger} \mathcal{H}_{\mathrm{SOC}} \Psi_{\mathbf{k}}, \quad (19)$$

where the matrices $\mathcal{H}_0$ and $\mathcal{H}_{\mathrm{SOC}}$ can be directly read off Eqs. (5) and (7). As for the interacting part, we start by projecting all possible electron-electron interactions in the spin and orbital loop-current channels:

$$H_{\mathrm{int}} = \left[\sum_{i\mathbf{q}\mu} \left(U_{E_{Mi}}^{M} \hat{M}_{E_{Mi}}^{\mu}(\mathbf{q}) \hat{M}_{E_{Mi}}^{\mu}(-\mathbf{q}) \right) \right.$$
$$\left. + U_{E_{Mi}}^{\Phi} \hat{\Phi}_{E_{Mi}}^{\mu}(\mathbf{q}) \hat{\Phi}_{E_{Mi}}^{\mu}(-\mathbf{q}) \right], \quad (20)$$

where the SDW and OLC bosonic operators are given by

$$\hat{M}_{E_{Mi}}^{\mu}(\mathbf{q}) = \sum_{\mathbf{k}} \Psi_{\mathbf{k}+\mathbf{q}}^{\dagger} \Upsilon_{E_{Mi},\mu}^{M} \Psi_{\mathbf{k}}, \quad (21)$$

$$\hat{\Phi}_{E_{Mi}}^{\mu}(\mathbf{q}) = \sum_{\mathbf{k}} \Psi_{\mathbf{k}+\mathbf{q}}^{\dagger} \Upsilon_{E_{Mi},\mu}^{\Phi} \Psi_{\mathbf{k}}. \quad (22)$$

Here, the hat indicates that the quantity is an operator. The bosonic vertices $\Upsilon_{E_{Mi},\mu}^{M}$ and $\Upsilon_{E_{Mi},\mu}^{\Phi}$ for each channel indicate how each order couples to the low-energy electrons. They are represented in terms of 12×12 matrices acting in the

enlarged spinor space and can be read off using Table I. For instance, for the order parameters belonging to the irreducible representations E_{M1}^{-}, the vertices are given by

$$\Upsilon_{E_{M1},-}^{M} = \begin{pmatrix} 0 & \tau^{\uparrow}\sigma^x & 0 \\ \tau^{\uparrow}\sigma^x & 0 & 0 \\ 0 & 0 & 0 \end{pmatrix} \quad (23a)$$

$$\Upsilon_{E_{M1},-}^{\Phi} = \begin{pmatrix} 0 & 0 & -i\tau^{\downarrow}\sigma^0 \\ 0 & 0 & 0 \\ i\tau^{\downarrow}\sigma^0 & 0 & 0 \end{pmatrix} \quad (23b)$$

with $\tau^{\uparrow} = \begin{pmatrix} 1 & 0 \\ 0 & 0 \end{pmatrix}$ and $\tau^{\downarrow} = \begin{pmatrix} 0 & 0 \\ 0 & 1 \end{pmatrix}$ acting in orbital doublet space and Pauli matrices σ^a acting in spin space. Note that each entry of the matrices above is itself a 4×4 matrix. The vertices of the remaining channels are listed in Appendix D for convenience. The effective interactions $U_{E_{Mi}}^{M}$ and $U_{E_{Mi}}^{\Phi}$ have contributions from interorbital and intraorbital on-site interactions, and will not be discussed here. Previous results have established that, for most of the parameter space, only the SDW state develops spontaneously (see for instance Ref. [17]).

We now introduced the bosonic fields $M_{E_{Mi}}^{\mu}$ and $\Phi_{E_{Mi}}^{\mu}$ via Hubbard-Stratonovich transformations of the quartic interaction terms. This decoupling makes the Hamiltonian quadratic in the fermions, which can now be integrated out, resulting in an effective free-energy functional for the two bosonic fields:

$$F[M,\Phi] = F_0 - \beta^{-1}\mathrm{tr}\ln[1 - \mathcal{G}V]$$
$$+ \sum_{i\mu q} \left[\frac{2}{U_{E_{Mi}}^{M}} |M_{E_{Mi}}^{\mu}(q)|^2 + \frac{2}{U_{E_{Mi}}^{\Phi}} |\Phi_{E_{Mi}}^{\mu}(q)|^2 \right]$$
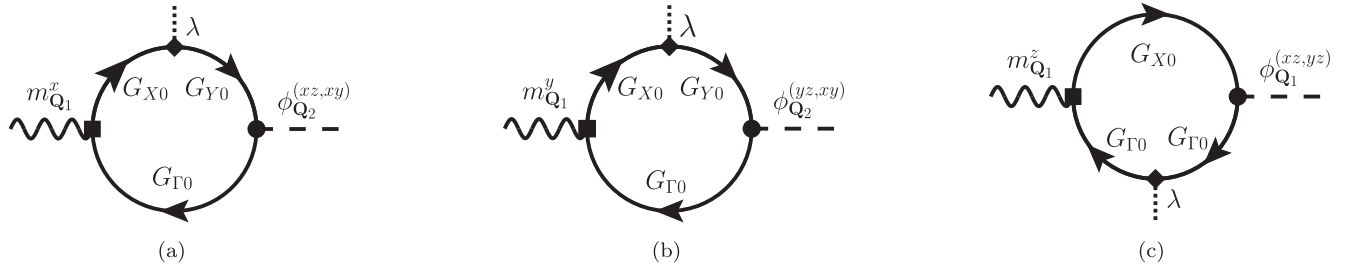$$(24)$$

FIG. 2. Microscopic representation of the coupling coefficient $g_{E_{Mi}}^{\mu}(\lambda)$ in terms of Feynman diagrams coupling spin density-wave and orbital loop-current orders. Wavy and dashed lines represent SDW and OLC current fields, respectively, whereas dotted lines refer to the spin-orbit interaction. $G_{\Gamma,0}$, G_{X0}, G_{Y0} represent fermionic propagators of electronic states residing at the three different pockets of the Brillouin zone. The vertices for the coupling between electronic and bosonic degrees of freedom and the SOC are represented by a square, a circle, and a diamond, respectively. (a) Coupling between the E_{M1}^{-} fields $m_{\mathbf{Q}_1}^{x}$ and $\phi_{\mathbf{Q}_2}^{(xz,xy)}$, (b) Coupling between the E_{M2}^{-} fields $m_{\mathbf{Q}_1}^{y}$ and $\phi_{\mathbf{Q}_2}^{(yz,xy)}$, and (c) Coupling between the E_{M3}^{+} fields $m_{\mathbf{Q}_1}^{z}$ and $\phi_{\mathbf{Q}_1}^{(xz,yz)}$.

with $q = (i\nu_n, \mathbf{q})$ denoting bosonic Matsubara frequency $\nu_n = 2n\pi T$ and momentum $\mathbf{q}$. The noninteracting fermionic propagator, defined in the 12-dimensional enlarged spinor space, is given by:

$$\mathcal{G}^{-1} = i\omega_n \mathbb{I} - (\mathcal{H}_0 + \mathcal{H}_{\text{SOC}}) \qquad (25)$$

with $\omega_n = (2n + 1)\pi T$ denoting a fermionic Matsubara frequency. The interaction term V is given in terms of the vertex functions by

$$V = \sum_{i\mu} \left(\Upsilon_{E_{Mi},\mu}^{M} M_{E_{Mi}}^{\mu} + \Upsilon_{E_{Mi},\mu}^{\Phi} \Phi_{E_{Mi}}^{\mu} \right). \qquad (26)$$

The trace runs over spin and orbital indices as well as momenta and frequencies of the electronic degrees of freedom.

Since the electronic states at the Γ and X/Y points fully decouple, even in the presence of spin-orbit coupling, we rewrite the noninteracting propagator $\mathcal{G}$ in the more convenient block-diagonal form:

$$\mathcal{G} = \begin{pmatrix} G_{\Gamma\Gamma} & 0 & 0 \\ 0 & G_{XX} & G_{XY} \\ 0 & G_{YX} & G_{YY} \end{pmatrix}. \qquad (27)$$

Near the Γ point, we have

$$G_{\Gamma\Gamma} = \left(G_{\Gamma,0}^{-1} - \Lambda_{\Gamma}^{\text{SOC}} \right)^{-1} \qquad (28)$$

with:

$$G_{\Gamma,0}^{-1} = i\omega_n \mathbb{I} - \epsilon_{\mathbf{k}}^{\Gamma} \qquad (29)$$

and $\Lambda_{\Gamma}^{\text{SOC}}$ as defined in Eq. (8a). Note that the momentum and spin indices are dropped for the sake of simplicity.

At the X and Y points, the electronic states of both Fermi pockets are coupled to each other by the spin-orbit interaction. Defining:

$$G_{X,0}^{-1} = i\omega_n \mathbb{I} - \epsilon_{\mathbf{k}}^{X}, \quad G_{Y,0}^{-1} = i\omega_n \mathbb{I} - \epsilon_{\mathbf{k}}^{Y} \qquad (30)$$

we have the block-diagonal matrix:

$$\begin{pmatrix} G_{XX} & G_{XY} \\ G_{YX} & G_{YY} \end{pmatrix}$$
$$= \left[\begin{pmatrix} G_{X,0}^{-1} & 0 \\ 0 & G_{Y,0}^{-1} \end{pmatrix} - \begin{pmatrix} 0 & \Lambda_M^{\text{SOC}} \\ (\Lambda_M^{\text{SOC}})^{\dagger} & 0 \end{pmatrix} \right]^{-1} \qquad (31)$$

with Λ_M^{SOC} given in Eq. (8b).

We are now in position to expand the logarithm in Eq. (24) in powers of the bosonic fields using the identity $\ln(1 - GV) = -\sum_{n=1}^{\infty} \frac{1}{2n}(GV)^{2n}$. Focusing on the terms that are second order in the bosonic fields $M_{E_{Mi}}^{\mu}$ and $\Phi_{E_{Mi}}^{\mu}$, we find the bilinear coupling

$$\delta F = \sum_{i\mu q} g_{E_{Mi}}^{\mu}(\lambda) \, \Phi_{E_{Mi}}^{\mu}(-q) M_{E_{Mi}}^{\mu}(q) + \text{c.c.} \qquad (32)$$

with

$$g_{E_{Mi}}^{\mu}(\lambda) = \tfrac{1}{2} \text{tr} \big[\mathcal{G} \Upsilon_{E_{Mi},\mu}^{\Phi} \mathcal{G} \Upsilon_{E_{Mi},\mu}^{M} \big], \qquad (33)$$

where the trace runs over orbital doublet and spin space indices, as well as momentum and frequency. It is clear why this term vanishes in the absence of SOC: the SDW vertex $\Upsilon_{E_{Mi},\mu}^{M}$ has a Pauli matrix, whereas the OLC vertex $\Upsilon_{E_{Mi},\mu}^{\Phi}$ does not. If there is no SOC, then the noninteracting Green's functions $\mathcal{G}$ are also spin independent, implying that the trace over spin indices gives zero.

To better highlight the effects of the SOC, we perform an expansion in powers of λ. A graphical representation of the microscopic process generating $g_{E_{Mi}}^{\mu}$ in terms of Feynman diagrams of three of the six introduced orders is depicted in Fig. 2. Note that for a coupling between static and spatially uniform orders, which is of interest in this work, the external momentum and frequency in the evaluation of Eq. (33) are set to zero. The calculation of the coupling constants is now straightforward. For E_{M1}^{-}, where $m_{\mathbf{Q}_1}^{x}$ couples to $\phi_{\mathbf{Q}_2}^{(xz,xy)}$, we obtain:

$$\begin{aligned} g_{E_{M1}}^{-}(\lambda) &= \frac{1}{2} \text{tr}[G_{XY}(i\tau^{\downarrow}\sigma^{0})G_{\Gamma}(\tau^{\uparrow}\sigma^{x}) \\ &\quad - G_{\Gamma}(i\tau^{\downarrow}\sigma^{0})G_{YX}(\tau^{\uparrow}\sigma^{x})] \\ &\approx \frac{1}{2} \text{tr}[G_{X,0}\Lambda_M^{\text{SOC}}G_{Y,0}(i\tau^{\downarrow}\sigma^{0})G_{\Gamma,0}(\tau^{\uparrow}\sigma^{x}) \\ &\quad - G_{\Gamma}(i\tau^{\downarrow}\sigma^{0})G_{Y,0}(\Lambda_M^{\text{SOC}})^{\dagger}G_{X,0}(\tau^{\uparrow}\sigma^{x})] \\ &= -\lambda \int_k [G_{X,0}]_{11}[G_{Y,0}]_{22}[G_{\Gamma,0}]_{21}, \qquad (34) \end{aligned}$$

where we approximated $G_{XY} \approx G_{X,0}\Lambda_M^{\text{SOC}}G_{Y,0}$ and $G_{YX} \approx G_{Y,0}(\Lambda_M^{\text{SOC}})^{\dagger}G_{X,0}$. In the last line we performed the trace

over orbital doublet and spin space and left the remaining integration over momentum and frequency symbolized by $\int_k = T \sum_{\omega_n} \int \frac{d\mathbf{k}}{(2\pi)^2}$.

The evaluations of the other coefficients are analogous. For E_{M2}^- we find:

$$g_{E_{M2}^-}(\lambda) \approx \lambda \int_k [G_{X,0}]_{12}[G_{Y,0}]_{12}[G_{\Gamma,0}]_{11}, \qquad (35)$$

whereas for E_{M3}^+

$$g_{E_{M3}^+}(\lambda) \approx \lambda \int_k [G_{X,0}]_{11}([G_{\Gamma,0}]_{21}[G_{\Gamma,0}]_{21}$$
$$- [G_{\Gamma,0}]_{11}[G_{\Gamma,0}]_{22}). \qquad (36)$$

In all cases, we find that $g_{E_{Mi}}^\mu(\lambda = 0) = 0$, as expected. The bilinear coupling in the free energy ensures that $\Phi_{E_{Mi}}^\mu$ becomes nonzero once $M_{E_{Mi}}^\mu$ orders. Indeed, the full free-energy expansion becomes (assuming real fields):

$$F[M, \Phi] = g(\lambda)\Phi M + \frac{r_M}{2}M^2$$
$$+ \frac{r_\Phi}{2}\Phi^2 + \frac{u_M}{4}M^4, \qquad (37)$$

where we dropped the indices E_{Mi}, μ for simplicity of notation. The terms r_M and r_Φ trigger the onset of long-range order in the usual manner, and $u_M > 0$. Because Φ does not usually order on its own, r_Φ remains positive and we can keep the free-energy expansion to quadratic order in Φ. Minimization of the free energy gives:

$$\Phi = -\frac{g(\lambda)}{r_\Phi} M \qquad (38)$$

showing that $M \neq 0$ gives $\Phi \neq 0$. Note also that, once Φ is integrated out, the magnetic free energy changes to:

$$F[M] = \left(\frac{r_M}{2} - \frac{g^2(\lambda)}{r_\Phi}\right)M^2 + \frac{u_M}{4}M^4, \qquad (39)$$

which demonstrates that the SDW transition temperature is enhanced.

To give a rough estimate of the magnitude of the OLC order parameter induced by the SDW order parameter, Eq. (38), we consider how the relevant energy scales of the problem enter in the combination $g(\lambda)/r_\Phi$ that determines the ratio Φ/M. Although numerical value may be obtained by fitting the microscopic parameters such as the electronic dispersion and interaction parameters to experiments or first-principle calculations, this is not the scope of this work. To estimate the microscopic coupling g, we note that it is generically given by the SOC times a product of three fermionic Green's functions, see Eqs. (34)–(36) of type

$$g(\lambda) = \lambda T \sum_{\omega_n} \int_{\mathbf{k}} G_{i,0}G_{j,0}G_{k,0}. \qquad (40)$$

Using the general form $G_i^{-1} = i(2n+1)\pi T - \epsilon_{i,\mathbf{k}}$ and changing $\int \frac{d\mathbf{k}}{(2\pi)^2} = \rho_F \int d\epsilon$, we obtain

$$g(\lambda) \approx A\frac{\lambda}{T\epsilon_F}, \qquad (41)$$

where the numerical factor A depends on the details of band structure. Here, the density of states at the Fermi level was approximated by the inverse Fermi energy $\rho_F \sim \epsilon_F^{-1}$. To estimate the parameter r_Φ, we compare it to the quadratic Ginzburg-Landau coefficient of the SDW degrees of freedom, r_M, see Eq. (37). The difference between them is expected to be dominated, in the weak-coupling regime, by the difference in the effective electron-electron interaction strengths projected in the corresponding channels, denoted by U_M (for SDW) and U_Φ (for OLC):

$$r_\Phi - r_M \approx \frac{1}{U^\Phi} - \frac{1}{U^M}. \qquad (42)$$

Near the SDW transition temperature T_M, $r_M \approx 0$. Thus, the estimate for the ratio between the OLC and SDW order parameters is:

$$\frac{g(\lambda)}{r_\Phi} \approx A\frac{\lambda}{T_M}\frac{U^\Phi}{\epsilon_F}\frac{U^M}{U^M - U^\Phi}. \qquad (43)$$

Therefore, the ratio Φ/M depends on four factors: There is a dimensionless factor A depending on the details of the band structure. The second factor is the ratio between the SOC energy scale and SDW transition temperature. A rough estimate for the iron-based systems with $\lambda \approx 10$ meV and $T_M \approx 100$ K yields $\frac{\lambda}{T_M} \approx 1$. The third factor is the ratio between the OLC interaction strength and Fermi energy, which we expect to be small in a weak-coupling expansion $\frac{U^\Phi}{\epsilon_F} \ll 1$. The fourth factor depends on the difference between the interaction strengths in the OLC and SDW channels: For $U^\Phi \ll U^M$, $\frac{U^M}{U^M - U^\Phi} \approx 1$ and the induced OLC is expected to be small $\Phi \ll M$. However, if the system is sufficiently close to an OLC instability $U_\Phi \lesssim U_M$, the induced OLC can be comparable with the SDW, $\Phi \sim M$.

V. EXPERIMENTAL MANIFESTATIONS OF ORBITAL LOOP-CURRENT ORDER

The previous sections show that OLC is induced by SDW. An important issue is about the impact of OLC to the physics of the iron-based superconductors. In this section, we discuss two direct experimental manifestations of OLC that can in principle be detected with appropriate probes. Detection of these effects and of their amplitudes will allow one to assess the significance of these degrees of freedom to the properties of these systems.

A. Induced magnetic moments on the pnictogen/chalcogen sites

An obvious manifestation of static loop currents is the generation of magnetic fields, according to the Biot-Savart law of classical electrodynamics. To determine the magnetic field distributions corresponding to each loop-current configuration, we employ symmetry-based arguments, i.e., the induced magnetic fields must transform as the underlying loop-current pattern under the symmetry operations of the lattice. We follow a procedure similar to Ref. [33].

TABLE III. Transformation behavior of the irreducible representations E_{Mi} for the point symmetry operations discussed in the main text, $\sigma_x^{As/Se}$, $\sigma_y^{As/Se}$, $\sigma_z\sigma_x^{Fe}$, and $\sigma_z\sigma_y^{Fe}$.

irrep	$\sigma_x^{As/Se}$	$\sigma_y^{As/Se}$	$\sigma_z\sigma_x^{Fe}$	$\sigma_z\sigma_y^{Fe}$
E_{M1}	$\begin{bmatrix} -1 & 0 \\ 0 & -1 \end{bmatrix}$	$\begin{bmatrix} -1 & 0 \\ 0 & -1 \end{bmatrix}$	$\begin{bmatrix} 1 & 0 \\ 0 & -1 \end{bmatrix}$	$\begin{bmatrix} -1 & 0 \\ 0 & 1 \end{bmatrix}$
E_{M2}	$\begin{bmatrix} 1 & 0 \\ 0 & 1 \end{bmatrix}$	$\begin{bmatrix} 1 & 0 \\ 0 & 1 \end{bmatrix}$	$\begin{bmatrix} -1 & 0 \\ 0 & 1 \end{bmatrix}$	$\begin{bmatrix} 1 & 0 \\ 0 & -1 \end{bmatrix}$
E_{M3}	$\begin{bmatrix} 1 & 0 \\ 0 & -1 \end{bmatrix}$	$\begin{bmatrix} -1 & 0 \\ 0 & 1 \end{bmatrix}$	$\begin{bmatrix} -1 & 0 \\ 0 & -1 \end{bmatrix}$	$\begin{bmatrix} -1 & 0 \\ 0 & -1 \end{bmatrix}$
E_{M4}	$\begin{bmatrix} -1 & 0 \\ 0 & 1 \end{bmatrix}$	$\begin{bmatrix} 1 & 0 \\ 0 & -1 \end{bmatrix}$	$\begin{bmatrix} 1 & 0 \\ 0 & 1 \end{bmatrix}$	$\begin{bmatrix} 1 & 0 \\ 0 & 1 \end{bmatrix}$

TABLE IV. Direction of the loop-current induced magnetic moments $\mathbf{B}_{ind}$ at Fe and pnictogen/chalcogen lattice sites as well as the spin magnetic moments $\boldsymbol{\mu}$ at the Fe lattice sites.

irrep	Loop-current induced moments $\mathbf{B}_{ind}$		Spin moments $\boldsymbol{\mu}$
	at Fe	at As/Se	at Fe
$\begin{pmatrix} E_{M1}^+ \\ E_{M1}^- \end{pmatrix}$	$\begin{pmatrix} \hat{\mathbf{B}}_y \\ \hat{\mathbf{B}}_x \end{pmatrix}_{Fe}$	$\begin{pmatrix} \hat{\mathbf{B}}_z \\ \hat{\mathbf{B}}_z \end{pmatrix}_{As}$	$\begin{pmatrix} \hat{\boldsymbol{\mu}}_y \\ \hat{\boldsymbol{\mu}}_x \end{pmatrix}_{Fe}$
$\begin{pmatrix} E_{M2}^+ \\ E_{M2}^- \end{pmatrix}$	$\begin{pmatrix} \hat{\mathbf{B}}_x \\ \hat{\mathbf{B}}_y \end{pmatrix}_{Fe}$	$-$	$\begin{pmatrix} \hat{\boldsymbol{\mu}}_x \\ \hat{\boldsymbol{\mu}}_y \end{pmatrix}_{Fe}$
$\begin{pmatrix} E_{M3}^+ \\ E_{M3}^- \end{pmatrix}$	$\begin{pmatrix} \hat{\mathbf{B}}_z \\ \hat{\mathbf{B}}_z \end{pmatrix}_{Fe}$	$\begin{pmatrix} \hat{\mathbf{B}}_x \\ \hat{\mathbf{B}}_y \end{pmatrix}_{As}$	$\begin{pmatrix} \hat{\boldsymbol{\mu}}_z \\ \hat{\boldsymbol{\mu}}_z \end{pmatrix}_{Fe}$

The point symmetry operations that will be used in the following analysis are given by mirror reflections cutting Fe and As/Se sites combined with horizontal reflections. At the As/Se lattice sites, there are mirror planes whose normals point along the x and y directions, denoted respectively by $\sigma_x^{As/Se}$ and $\sigma_y^{As/Se}$. At the Fe lattice sites, these mirror reflections are combined with reflections with respect to the horizontal Fe plane yielding the point symmetry operations $\sigma_z\sigma_x^{Fe}$ and $\sigma_z\sigma_y^{Fe}$. The transformation behavior of the four distinct irreducible representations E_{Mi} under these point symmetry operations are listed in Table III. The latter can be verified using the current pattern representations in Fig. 1, and were also given in Ref. [15]. For the subsequent analysis, note that whereas a current transforms as a vector, an induced magnetic field transforms as a pseudovector, meaning that the normal component remains invariant whereas in-plane components change sign under mirror reflections.

To illustrate the logic of the symmetry-based argument for the existence of induced magnetic moments introduced above, we discuss in detail loop currents, which transform as the irreducible representation E_{M1}. In the following, we denote the direction of induced magnetic moments by $\hat{\mathbf{B}}_\alpha = \frac{\mathbf{B}_{ind}}{|\mathbf{B}_{ind}|}$ with $\alpha = x, y, z$ representing the particular directions along the Fe-Fe bonds (x, y) or pointing out of plane (z). We are looking for a doublet of directions of induced magnetic moments $(\hat{\mathbf{B}}_\alpha, \hat{\mathbf{B}}_{\alpha'})^T$ that corresponds to loop currents of one irreducible representation. We find at the Fe and As/Se lattice, respectively,

$$\sigma_z\sigma_x^{Fe}\begin{pmatrix} \hat{\mathbf{B}}_y \\ \hat{\mathbf{B}}_x \end{pmatrix}_{Fe} = \begin{pmatrix} \hat{\mathbf{B}}_y \\ -\hat{\mathbf{B}}_x \end{pmatrix}_{Fe}, \tag{44a}$$

$$\sigma_z\sigma_y^{Fe}\begin{pmatrix} \hat{\mathbf{B}}_y \\ \hat{\mathbf{B}}_x \end{pmatrix}_{Fe} = \begin{pmatrix} -\hat{\mathbf{B}}_y \\ \hat{\mathbf{B}}_x \end{pmatrix}_{Fe}, \tag{44b}$$

$$\sigma_x^{As/Se}\begin{pmatrix} \hat{\mathbf{B}}_z \\ \hat{\mathbf{B}}_z \end{pmatrix}_{As} = -\begin{pmatrix} \hat{\mathbf{B}}_z \\ \hat{\mathbf{B}}_z \end{pmatrix}_{As}, \tag{44c}$$

$$\sigma_y^{As/Se}\begin{pmatrix} \hat{\mathbf{B}}_z \\ \hat{\mathbf{B}}_z \end{pmatrix}_{As} = -\begin{pmatrix} \hat{\mathbf{B}}_z \\ \hat{\mathbf{B}}_z \end{pmatrix}_{As}, \tag{44d}$$

which transform consistently as the E_{M1} loop currents as indicated in Table III. We therefore conclude that these are

the directions of local magnetic moments at the Fe and As/Se lattice sites, which are induced by these particular orbital loop currents. It is straightforward to verify that this is the only possible distribution of moments that is allowed by symmetry.

Our results for the directions of possible induced magnetic moments for all types of loop-current orders are presented in Table IV. Note that they agree with the As/Se magnetic moments discussed in Ref. [15] derived solely on symmetry considerations. We find that at Fe lattice sites the induced magnetic fields are pointing in the same direction as the magnetic moments of the corresponding SDW orders. This is not surprising since the SDW and OLC orders share the same symmetry properties. It can also be traced back to the physical fact that the two orders couple via these moments. However, there are also induced magnetic fields located at the pnictogen/chalcogenide (As/Se) lattice sites, which represent a unique signature of the distinct loop-current patterns.

To establish a link between the derived schematic current pattern shown in Fig. 1 and the direction of the induced magnetic fields, one has to include the actual current flow via the As/Se lattice sites. This immediately gives rise to orbital independent current pattern for E_{M1}^μ and E_{M3}^μ loop-current orders as depicted in Fig. 3(a) and 3(c), respectively. In case of E_{M2}^μ current order we encounter a problem: The net charge flow between Fe lattice sites sums up to zero as seen in Fig. 3(b). This can traced back to the fact that the E_{M2}^μ current pattern transform evenly under point symmetry operations with respect to the Fe lattice sites (see Table III). Thus, a refined analysis, which takes higher-order Fe-Fe hopping processes into account as conducted in the previous section, would not yield any solution and only an explicit consideration of electronic degrees of freedom of pnictogen/chalcogenide atoms would remedy this problem. Here, we will use the symmetry properties of the E_{M2}^μ irreducible representation to derive an effective current pattern: Besides the transformation behaviors under point symmetry operations, we require loop currents that preserve local charge conservation and posses ordering momentum $\mathbf{Q}_j$. The result is depicted in Fig. 3(b).

Besides the effective current flow pattern, the induced magnetic fields in combination with one realization of the responsible loop currents are visualized in Fig. 3. The out-of-plane position and the alternating stacking of As/Se lattice sites are crucial features and allow for in-plane magnetic fields.
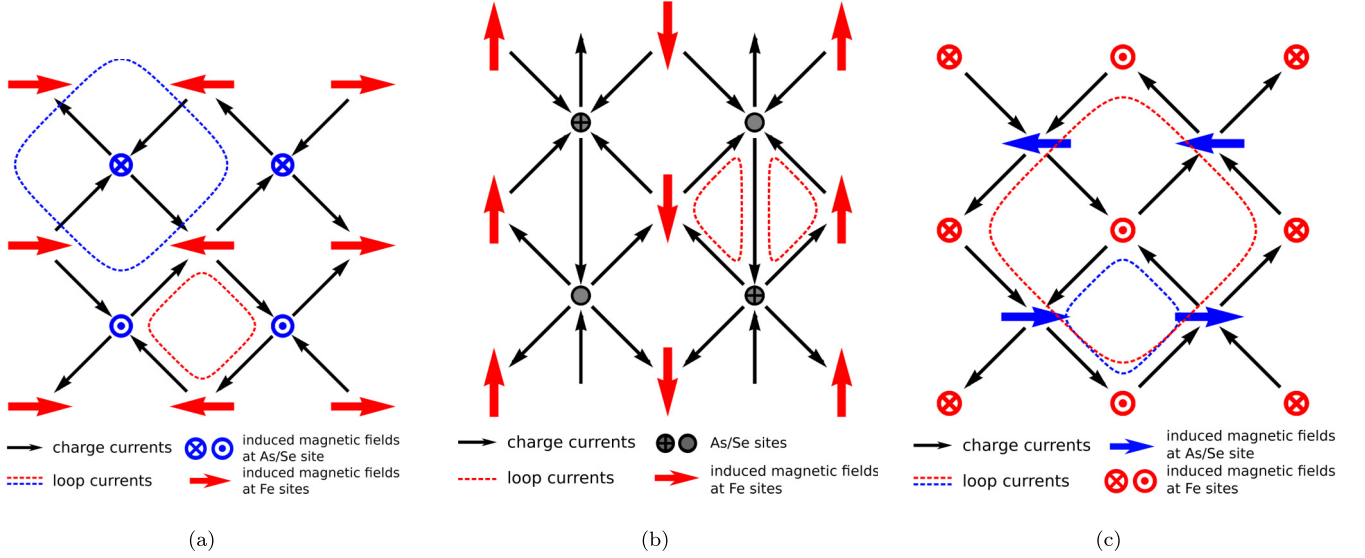
FIG. 3. Magnetic moments induced by different loop-current configurations. Note that, in contrast to Fig. 1, here we show explicitly the charge current path going through the As/Se site (black arrows). The corresponding closed loops that induce magnetic moments at the Fe sites and at the As/Se sites are shown by dashed red and blue curves, respectively. Accordingly, the induced magnetic moments at the Fe and As/Se sites are represented by red and blue arrows, respectively. Recall that the As/Se lattice sites are positioned above and below the horizontal Fe plane in a staggering pattern. This feature of the crystal lattice is what gives rise to in-plane induced magnetic moments at the Fe/Se sites. (a) Loop current order E_{M1}^- : $\phi_{Q_2}^{(xz,xy)}$, (b) Loop current order E_{M2}^- : $\phi_{Q_2}^{(yz,xy)}$, and (c) Loop current order E_{M3}^+ : $\phi_{Q_1}^{(xz,yz)}$.

They also provide a physical understanding of the fact that loop-current orders, which are composed out of evenly and oddly transforming orbitals, couple to magnetic orders with different pseudocrystal momentum as discussed in Sec. II: The momentum of the induced magnetic fields is shifted by (π,π) due to the alternate stacking of As/Se lattice sites.

We now estimate the magnitude of the induced magnetic fields at the As/Se sites. Given the area of the loop current and the magnitude of the current, we can obtain the corresponding magnetic moment in a straightforward way:

$$\mu_{\text{OLC}} = A_\perp |\langle \hat{\mathbf{j}} \rangle| \sim \frac{A_\perp et}{\hbar} \Phi \qquad (45)$$

with $A_\perp$ being the area enclosed by the loop current $\langle \hat{\mathbf{j}} \rangle$ projected onto the direction of the magnetic moment. For magnetic moments lying out of plane, $A_\perp \sim a_{\text{Fe}}^2$, while for moments lying in plane, $A_\perp \sim a_{\text{Fe}} a_{\text{Pn}}$ where a_{Fe} is the Fe-Fe lattice spacing and a_{Pn} denotes the out-of-plane position of the pnictogen/chalcogen lattice sites. In the last step, we used the relationship between the average current and the OLC order parameter $|\langle \hat{\mathbf{j}} \rangle| \sim \frac{et}{\hbar} \Phi$ as discussed in the previous section, with t being some dominant kinetic energy scale of the electronic system. With the expression for the magnetic moments we approximate the induced magnetic field strength to

$$B_{\text{ind}} = \frac{2\mu_{\text{OLC}}}{cr^3} \sim \frac{A_\perp et}{c\hbar a_{\text{Fe}}^3} \Phi. \qquad (46)$$

For a quantitative statement we compare the system of the Fe-based superconductors to that of the cuprates superconductors. In those systems the induced magnetic field strength due to loop currents was estimated to be $B_{\text{Cu}} \sim 100-1000$ G [33]. In comparison, the typical energy scales in the Fe-based systems are one order of magnitude smaller $\frac{t_{\text{Fe}}}{t_{\text{Cu}}} \sim 0.1$. Thus,

we expect the induced magnetic field strength to be of order $B_{\text{ind}} \sim 10-100$ G.

An important issue is about how to detect these induced fields $\mathbf{B}_{\text{ind}}$ on the As/Se sites. NMR is a natural candidate to detect local fields, particularly since it can be done on the As and Se nuclei. However, the internal field measured by NMR also has contributions from the hyperfine field $\mathbf{B}_{\text{hf}}$ arising due to the coupling between the As/Se nuclei spins and the electronic Fe spins. Not surprisingly, the directions of these hyperfine fields $\mathbf{B}_{\text{hf}}$ are exactly the same as the directions of the fields induced by the loop currents, $\mathbf{B}_{\text{ind}}$ (see, for instance, Ref. [34]). Thus, unambiguously distinguishing the fields generated by the loop currents from the fields generated by the hyperfine nuclei-spins coupling is a difficult task. Instead of NMR, x-ray scattering may provide more unambiguous signatures of the fields induced by the loop currents. First, because the loop currents are extended objects, they will likely produce form factors that are rather distinct from those arising from pointlike moments. Second, the x rays can be tuned to the As absorption edge, thus providing information about the electronic magnetization of the As atoms only. Recently, x-ray absorption measurements tuned to the As K edge were performed to unveil ferromagnetic order in the As sites of materials closely related to the 122 iron pnictides [35].

B. Orbitally selective band splittings

A direct manifestation of OLC order is on the electronic spectrum near the high-symmetry points, which can be probed experimentally using ARPES [20,36]. To discuss this effect, it is convenient to refer to the coordinate system corresponding to the 2-Fe Brillouin zone. Recall that both the X and Y points of the 1-Fe Brillouin zone are folded onto the M point of the 2-Fe Brillouin zone (see inset of Fig. 4). Since the M point
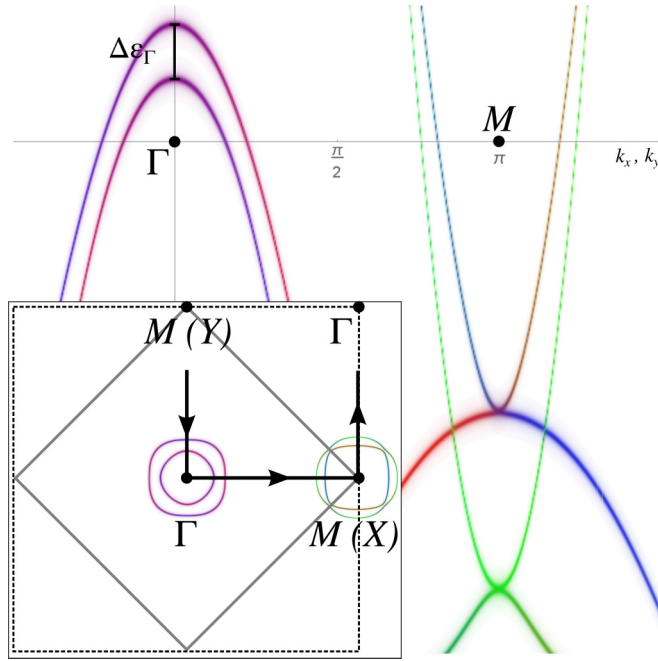
FIG. 4. Electronic band dispersion in the tetragonal phase in the presence of spin-orbit coupling. The latter gives rise to a strong mixing of electronic states and a band splitting of $|\lambda|$ at the Γ point, but does not affect the doublets at the M point. The orbital content of the electronic states is represented by different colors: Blue and red correspond to xz and yz orbitals, respectively, while green, to the xy orbital. Here, the electronic states are represented in the two Fe Brillouin zone, where the X and Y points are both folded onto the M point. The dispersions plotted correspond to the cuts indicated in the inset. The Fermi surface is also shown in the inset.

only admits two-dimensional irreducible representations, all electronic states at the M point are doubly degenerate (on top of the standard Kramers degeneracy). This degeneracy holds even in the presence of spin-orbit coupling λ. In particular, the two lowest-energy doublets at M correspond to $[\epsilon^X_{\mathbf{k}=0}]_{11} = [\epsilon^Y_{\mathbf{k}=0}]_{22} = \epsilon_1$ and $[\epsilon^X_{\mathbf{k}=0}]_{22} = [\epsilon^Y_{\mathbf{k}=0}]_{11} = \epsilon_3$, with $|\epsilon_3| > |\epsilon_1|$, and the matrix elements corresponding to the noninteracting Hamiltonian of Eq. (5). Note that the off-diagonal elements $[\epsilon^X_{\mathbf{k}=0}]_{12} = [\epsilon^Y_{\mathbf{k}=0}]_{12} = 0$ vanish at the M point. The Γ point also has one energy doublet, $[\epsilon^\Gamma_{\mathbf{k}=0}]_{11} = [\epsilon^\Gamma_{\mathbf{k}=0}]_{22} = \epsilon_\Gamma$, associated with the two-dimensional irreducible representation E_g at the zone center. In contrast to the doublets at M, however, this doublet is split by the SOC (see Fig. 4).

In terms of the orbitals, which are good quantum numbers at the M point, the existence of the doublet ϵ_1 (ϵ_3) is a consequence of the fact that the xz orbital (xy orbital) on-site energy at X is equivalent to the yz orbital (xy orbital) on-site energy energy at Y. Because long-range SDW and OLC orders mix these orbitals, they lead to splittings of the corresponding doublets. Now because the orbitals involved in the SDW order parameter $M^\mu_{E_{Mi}}$ are not necessarily the same as those involved in the OLC order parameter $\Phi^\mu_{E_{Mi}} \neq 0$, each order parameter will affect differently each doublet. In particular, because intraorbital magnetism can only involve xz and yz orbitals (assuming, of course, that there is not a xy hole pocket at Γ, as it happens in a few iron pnictides), the onset of long-range

SDW order can only split the ϵ_1 doublet. However, if the OLC order parameter belongs to the E_{M1} or E_{M2} irreducible representations, it involves also the xy orbital, as shown in Table I. As a result, it leads to a splitting of the ϵ_3 doublet, but not of ϵ_1.

To make this analysis quantitative, we assume nonzero values for $M^\mu_{E_{Mi}} \neq 0$ and $\Phi^\mu_{E_{Mi}} \neq 0$ and diagonalize the quadratic Hamiltonian $H_0 + H_{\mathrm{SOC}} + H_{\mathrm{SDW}} + H_{\mathrm{OLC}}$ for each different irreducible representation. In Fig. 5, we show the corresponding band dispersions in the SDW+OLC state for three different possible types of order. Focusing at the doublets at the Γ and M points, we can obtain all induced splittings analytically to leading order in the SOC λ, in the SDW order parameter M, and in the OLC order parameter Φ. When the latter transform as components of the irreducible representations E_{M1} and E_{M2}, we find the following leading-order band splittings

$$\Delta\epsilon_\Gamma \approx |\lambda| \tag{47a}$$

$$\Delta\epsilon_1 \approx \frac{M^2}{|\epsilon_\Gamma - \epsilon_1|} \tag{47b}$$

$$\Delta\epsilon_3 \approx \frac{\Phi^2}{|\epsilon_\Gamma - \epsilon_3|}. \tag{47c}$$

The fact that the orders that transform as E_{M1} and E_{M2} yield equivalent results is attributed to the fact that both orders couple orbitals at Γ to the xy orbital at X/Y. A difference in band shifts appear only in higher order in the order parameters. Since $\Phi = -\chi_\Phi g(\lambda)M$, where $\chi_\Phi^{-1} = r_\Phi$ is the OLC susceptibility, the ratio between the doublet splittings at the M point provide an interesting way to estimate the coupling between the SDW and OLC orders:

$$\Delta\epsilon_3/\Delta\epsilon_1 \approx \chi_\Phi^2 g^2(\lambda) \frac{|\epsilon_\Gamma - \epsilon_1|}{|\epsilon_\Gamma - \epsilon_3|}. \tag{48}$$

For coupled SDW-OLC orders that transform as E_{M3}, the band splittings become, to leading order

$$\Delta\epsilon_\Gamma \approx |\lambda| - 2\frac{M\Phi}{|\epsilon_\Gamma - \epsilon_1|} \tag{49a}$$

$$\Delta\epsilon_1 \approx \frac{M^2 + \Phi^2}{|\epsilon_\Gamma - \epsilon_1|} \tag{49b}$$

$$\Delta\epsilon_3 \approx 0. \tag{49c}$$

In comparing these results with ARPES experiments, one has to keep in mind that orbital order also leads to splittings of these doublets [14]. However, for orders that transform as E_{M1} and E_{M2}, the additional splitting of the doublet ϵ_3 represents an unique signature since it is unaffected by orbital and intraorbital spin magnetic orders involving predominantly xz/yz orbitals. Thus, proper consideration of this effect is needed to extract the doublet splittings produced only by SDW and OLC order.

The onset of OLC order also impacts the reconstruction of the Fermi surface in the magnetically ordered state, which can also be probed by ARPES. Specifically, due to the interorbital nature of the OLC orders, additional parts of the Fermi surface can be gapped, as compared to the case in which only intraorbital SDW is present, depicted in Fig. 6(a). Figures 6(b)–6(d) depict our results for the reconstructed Fermi surface assuming SDW and OLC order parameters of equal magnitudes, $M = \Phi$. Note that, in the case of order parameters
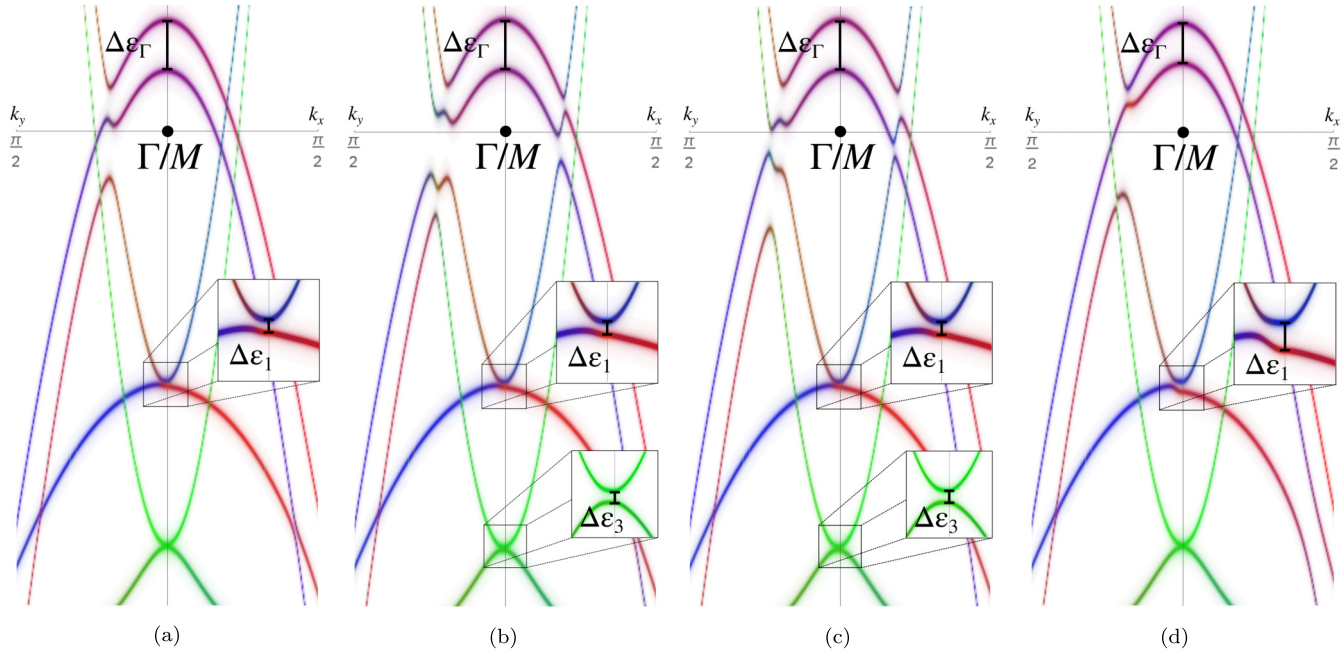
FIG. 5. Reconstructed electronic dispersions in the SDW phase for (a) vanishing and (b)–(d) nonvanishing coupling to the OLC order parameter. In the absence of SDW-OLC coupling, the reconstructed electronic structures associated with each SDW irreducible representation are the same (a). However, for finite SDW-OLC coupling, the resulting band dispersion is different for the (b), (c) $E_{M1,M2}$ and (d) E_{M3} representations. The dispersions plotted correspond to the cuts displayed in the inset of Fig. 4. The insets zoom in on the splittings of the energy doublets at the M point associated with each case. The electronic dispersion parameters are taken from Ref. [15] (see also Appendix C). To highlight the main features caused by each electronic reconstruction, the spin-orbit coupling is set to $\lambda = 80$ meV, the SDW order parameter to $M = 65$ meV, and the induced OLC order parameter, to $\Phi = M$. (a) SDW order for vanishing SDW-OLC coupling, (b) Coupled E_{M1}^{-} SDW and OLC orders, (c) Coupled E_{M2}^{-} SDW and OLC orders, and (d) Coupled E_{M3}^{+} SDW and OLC orders.

belonging to the $E_{M1,M2}$ representations, the onset of OLC order leads to an additional gapping of the Fermi surface along one direction. However, in the case of E_{M3} order, the Fermi surface remains very similar as the case without OLC order.

It is important to point out that the expressions derived in this section are valid if intraorbital magnetism involves only the xz/yz orbitals. For the cases where intraorbital magnetism involving also the xy orbital appears, which is presumably the case when the additional xy hole pocket is present, the situation changes. This is because the xy SDW order parameter also leads to splitting of the ϵ_3 doublet, which may mask or make it harder to distinguish the contribution arising from the OLC order parameter.
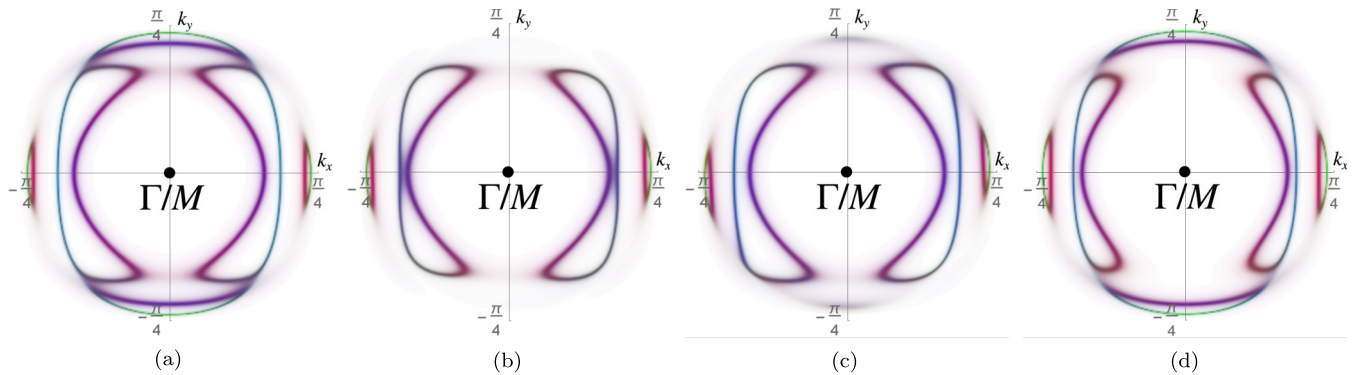

FIG. 6. Reconstructed Fermi surfaces corresponding to the band dispersions shown in Fig. 5. (a) corresponds to the SDW phase with vanishing SDW-OLC coupling, and is the same for all three irreducible representations of the SDW order parameter. (b)–(d) correspond to a nonvanishing SDW-OLC coupling. Note that, for the case of the $E_{M1,M2}$ representations, there is additional Fermi surface gapping as compared to the case of the E_{M3} representation and the case of vanishing SDW-OLC coupling. The parameters are the same as in Fig. 5. (a) SDW order for vanishing SDW-OLC coupling, (b) Coupled E_{M1}^{-} SDW and OLC orders, (c) Coupled E_{M2}^{-} SDW and OLC orders, and (d) Coupled E_{M3}^{+} SDW and OLC orders.

VI. CONCLUSIONS

In this paper, we showed that the onset of long-range SDW order belonging to one of two-dimensional irreducible representations E_{M_i} of the space group describing a generic iron -pnictide/chalcogenide plane must trigger an orbital loop-current order belonging to the same irreducible representation. Such a coupling between these two types of order is mediated by the spin-orbit interaction, which has been experimentally found to be sizable in these materials. Each irreducible representation implies different patterns of loop-current order, as they only allow very specific combination of charge flow between the Fe orbitals. For instance, the most widely realized magnetic ground state in the iron-based superconductors is the stripe SDW state belonging to the E_{M1} irreducible representation. It corresponds to stripes of parallel spins whose magnetic moments are parallel to the ordering vectors $\mathbf{Q}_1 = (\pi, 0)$ or $\mathbf{Q}_2 = (0, \pi)$. The corresponding OLC patterns have ordering vectors $\mathbf{Q}_2 = (0, \pi)$ or $\mathbf{Q}_1 = (\pi, 0)$, respectively, and involve charge transfer between neighboring Fe yz/xz and xy orbitals. Thus, even though the intraorbital SDW order affects directly only the xz and yz orbitals, it indirectly impacts also the xy orbital via the induced secondary interorbital OLC order. We note that, by symmetry, OLC order is also induced by other types of magnetic ground states, such as the C_4 double-$\mathbf{Q}$ magnetic phases observed in certain hole-doped pnictides [5–8].

In our considerations, we assumed that the microscopic electronic interactions always promote SDW order, of which the OLC order is just a byproduct. This seems to be the case according to Hartree-Fock [30] and renormalization group calculations [37]. It remains to be seen, however, whether the OLC order can ever become the leading instability of the system. In this case, besides OLC order, OLC fluctuations would become important, which can possibly affect nematicity [25] and even superconductivity. Note that, since the SDW and OLC order parameters share the same symmetry properties, both their fluctuations promote sign-changing s^{+-} superconductivity. Interestingly, other types of loop-current orders have been proposed in different correlated systems, most notably cuprates [27,28], in which the order is however considered as leading instability, and iridates [38]. Given that these are also multiorbital systems, it is interesting to explore whether any of the effects unveiled here could be relevant in those compounds.

Our finding epitomizes the unique entanglement between spin and orbital degrees of freedom in the iron-based superconductors, beyond the well-established interconnection between nematicity and ferro-orbital order [39,40]. It also raises the important question of whether the induced OLC order has a strong impact on the microscopic properties of these materials. Up to date, to the best of our knowledge, all properties of the SDW state have been interpreted in terms of a magnetic order parameter and the accompanying ferro-orbital order. To elucidate the extent to which the OLC order parameter affects different observables will require a reanalysis of several of previous experimental results. Here, we focused on two distinct manifestations of OLC order that can be probed experimentally, namely, the magnetic field induced by the loop currents on the pnictogen/chalcogen site, and the splitting of the xy doublet of the band structure at the M point. Interestingly, the latter has been recently observed in FeSe, where, however, the usual SDW order is absent [36]. Another possible manifestation of the coupling between OLC and SDW is in the spin-wave spectrum, as spin excitations become mixed with loop-current excitations. Obviously, such an effect will be stronger the closer the system is to an spontaneous OLC instability. Finally, since superconductivity is observed to coexist microscopically with SDW order in some iron-based compounds, an interesting open issue is how OLC order can impact this unique thermodynamic state.

APPENDIX A: NOTATION GUIDE

For convenience, here we provide a summary of the different quantities defined throughout the paper. Table V displays the objects defined in the Fe $3d$ orbital space. Table VI presents the quantities defined in terms of irreducible representations of the $P4/nmm$ space group, which describes a generic iron pnictogen/chalcogen plane. Finally, Table VII displays the quantities defined in the extended spinor space that describes the low-energy electronic model used throughout the text.

APPENDIX B: CLASSIFICATION OF SDW ORDER PARAMETERS INVOLVING d_{xy} ORBITALS

Table VIII shows how xy intraorbital SDW order parameters transform according to the irreducible representations $E_{Mi} : (E_{Mi}^+, E_{Mi}^-)$. Comparison with Table I in the main text shows that, for a given magnetic order parameter with ordering

TABLE V. Quantities defined in orbital space. Here, a and b are orbital indices referring to one of the three Fe $3d$ orbitals: xz, yz, and xy.

$d_{a,\mathbf{k}\sigma}$	Annihilation operator for an electron at orbital a with momentum $\mathbf{k}$ and spin σ.
$t_{ij}^{a,b}$	Amplitude for an electron hopping from site i, orbital a to site j, orbital b.
$\mathbf{m}_{\mathbf{Q}_i}^{(a,b)}$	Spin-density wave order parameter involving orbital a at momentum $\mathbf{k}$ and orbital b at momentum $\mathbf{k} + \mathbf{Q}_i$. Only two intraorbital combinations are considered in the main text, $\mathbf{m}_{\mathbf{Q}_1} \equiv \mathbf{m}_{\mathbf{Q}_1}^{(yz,yz)}$ and $\mathbf{m}_{\mathbf{Q}_2} \equiv \mathbf{m}_{\mathbf{Q}_1}^{(xz,xz)}$.
$\phi_{\mathbf{Q}_i}^{(a,b)}$	Orbital loop-current order parameter involving orbital a at momentum $\mathbf{k}$ and orbital b at momentum $\mathbf{k} + \mathbf{Q}_i$.

TABLE VI. Quantities defined in terms of irreducible representations of the $P4/nmm$ space group.

E_{Mi}	Two-dimensional irreducible representations of the $P4/nmm$ group at the $M = (\pi, \pi)$ point of the Brillouin zone corresponding to the 2-Fe unit cell. In this paper we focus on $i = 1, 2, 3$.
$M^\mu_{E_{Mi}}$	Spin-density wave order parameter expressed in terms of the two-dimensional irreducible representations E_{Mi}. Each doublet ($\mu = +, -$) corresponds to combinations of the components of $\mathbf{m}_{Q_i}$ introduced in Table V.
$\Phi^\mu_{E_{Mi}}$	Orbital loop-current order parameter expressed in terms of the two-dimensional irreducible representations E_{Mi}. Each doublet ($\mu = +, -$) corresponds to combinations of $\phi^{(a,b)}_{Q_i}$ introduced in Table V.

vector $\mathbf{Q}_i$ and moment direction m^α, the same types of OLC order are induced, regardless of whether the intraorbital SDW arises from xz/yz or xy orbitals.

APPENDIX C: ORBITAL DISPERSION RELATIONS

Here we give explicit expressions for the electronic dispersion relations introduced in Eq. (5):

$$\epsilon^\Gamma_{\mathbf{k}} = \begin{pmatrix} \epsilon_\Gamma + 2\frac{\mathbf{k}^2}{2m_\Gamma} + b(k_x^2 - k_y^2) & 4ck_xk_y \\ 4ck_xk_y & \epsilon_\Gamma + 2\frac{\mathbf{k}^2}{2m_\Gamma} - b(k_x^2 - k_y^2) \end{pmatrix},$$

$$\epsilon^X_{\mathbf{k}} = \begin{pmatrix} \epsilon_1 + 2\frac{\mathbf{k}^2}{2m_1} + a_1(k_x^2 - k_y^2) & -iv(\mathbf{k}) \\ iv(\mathbf{k}) & \epsilon_3 + 2\frac{\mathbf{k}^2}{2m_3} + a_3(k_x^2 - k_y^2) \end{pmatrix},$$

$$\epsilon^Y_{\mathbf{k}} = \epsilon^X_{\mathbf{k}}\big|_{k_x \to k_y, k_y \to -k_x}$$

with $v(\mathbf{k}) = 2vk_y + 2p_1k_y(k_y^2 + 3k_x^2) - 2p_2k_y(k_x^2 - k_y^2)$. The parameters $\epsilon_\Gamma, m_\Gamma, b, c$ for the dispersion at Γ and $\epsilon_1, m_1, a_1, \epsilon_3, m_3, a_3, v, p_1, p_2$ at the X and Y points can be found in Ref. [15].

APPENDIX D: VERTEX FUNCTIONS

The vertices introduced in Eqs. (21) and (22) for different orders are derived from their orbital and spin composition as stated in Table I. They are represented as matrices in enlarged orbital space $\Psi = (\psi_\Gamma, \psi_X, \psi_Y)^T$ and are given by

(i) E_{M1}:

$$\Upsilon^M_{E_{M1},+} = -\begin{pmatrix} 0 & 0 & \tau^- \sigma^y \\ 0 & 0 & 0 \\ \tau^+ \sigma^y & 0 & 0 \end{pmatrix},$$

$$\Upsilon^\Phi_{E_{M1},+} = \begin{pmatrix} 0 & i\tau^+ \sigma^0 & 0 \\ -i\tau^- \sigma^0 & 0 & 0 \\ 0 & 0 & 0 \end{pmatrix}$$

$$\Upsilon^M_{E_{M1},-} = \begin{pmatrix} 0 & \tau^\uparrow \sigma^x & 0 \\ \tau^\uparrow \sigma^x & 0 & 0 \\ 0 & 0 & 0 \end{pmatrix},$$

$$\Upsilon^\Phi_{E_{M1},-} = \begin{pmatrix} 0 & 0 & -i\tau^\downarrow \sigma^0 \\ 0 & 0 & 0 \\ i\tau^\downarrow \sigma^0 & 0 & 0 \end{pmatrix}$$

(ii) E_{M2}:

$$\Upsilon^M_{E_{M2},+} = -\begin{pmatrix} 0 & 0 & \tau^- \sigma^x \\ 0 & 0 & 0 \\ \tau^+ \sigma^x & 0 & 0 \end{pmatrix},$$

$$\Upsilon^\Phi_{E_{M2},+} = \begin{pmatrix} 0 & -i\tau^\downarrow \sigma^0 & 0 \\ i\tau^\downarrow \sigma^0 & 0 & 0 \\ 0 & 0 & 0 \end{pmatrix}$$

$$\Upsilon^M_{E_{M2},-} = \begin{pmatrix} 0 & \tau^\uparrow \sigma^y & 0 \\ \tau^\uparrow \sigma^y & 0 & 0 \\ 0 & 0 & 0 \end{pmatrix},$$

$$\Upsilon^\Phi_{E_{M2},-} = \begin{pmatrix} 0 & 0 & i\tau^+ \sigma^0 \\ 0 & 0 & 0 \\ -i\tau^- \sigma^0 & 0 & 0 \end{pmatrix}$$

TABLE VII. Quantities defined in the space of the low-energy electronic state spinors.

$\Psi_{\mathbf{k}} = (\psi_{\Gamma,\mathbf{k}}, \psi_{X,\mathbf{k}+\mathbf{Q}_1}, \psi_{Y,\mathbf{k}+\mathbf{Q}_2})^T$	Extended 12-dimensional electronic spinor. ψ_Γ, ψ_X, and ψ_Y are each four-dimensional spinors (two spins indices and two orbital indices) describing the low-energy states near the Γ, X, and Y points of the 1-Fe unit cell Brillouin zone.
Λ^{SOC}_Γ and Λ^{SOC}_M	Spin-orbit coupling vertices defined in the ψ_Γ and in the ψ_X/ψ_Y subspaces according to Eqs. (7) and (8a)–(8b).
$\Upsilon^M_{E_{Mi},\mu}$	Vertex describing the coupling between the spin density-wave order parameter $M^\mu_{E_{Mi}}$ and the electronic states described by the extended spinor $\Psi_{\mathbf{k}}$. The six 12×12 vertices are given in Appendix D.
$\Upsilon^\Phi_{E_{Mi},\mu}$	Vertex describing the coupling between the orbital loop-current order parameter $\Phi^\mu_{E_{Mi}}$ and the electronic states described by the extended spinor $\Psi_{\mathbf{k}}$. The six 12×12 vertices are given in Appendix D.

TABLE VIII. Possible spin density-wave orders containing electronic xy-orbital states and the corresponding OLC orders.

irrep of $P4/nmm$ space group	intraorbital spin order		orbital loop current order	
	field	orbital and spin comp.	field	orbital composition
$\begin{pmatrix} E_{M1}^{+} \\ E_{M1}^{-} \end{pmatrix}$	$\begin{pmatrix} m_{\mathbf{Q}_2}^{y} \\ m_{\mathbf{Q}_1}^{x} \end{pmatrix}$	$\begin{pmatrix} xy, \sigma^{y} \\ xy, \sigma^{x} \end{pmatrix}$	$\begin{pmatrix} \phi_{\mathbf{Q}_1}^{(yz,xy)} \\ \phi_{\mathbf{Q}_2}^{(xz,xy)} \end{pmatrix}$	$\begin{pmatrix} yz, xy \\ xz, xy \end{pmatrix}$
$\begin{pmatrix} E_{M2}^{+} \\ E_{M2}^{-} \end{pmatrix}$	$\begin{pmatrix} m_{\mathbf{Q}_2}^{x} \\ m_{\mathbf{Q}_1}^{y} \end{pmatrix}$	$\begin{pmatrix} xy, \sigma^{x} \\ xy, \sigma^{y} \end{pmatrix}$	$\begin{pmatrix} \phi_{\mathbf{Q}_1}^{(xz,xy)} \\ \phi_{\mathbf{Q}_2}^{(yz,xy)} \end{pmatrix}$	$\begin{pmatrix} xz, xy \\ yz, xy \end{pmatrix}$
$\begin{pmatrix} E_{M3}^{+} \\ E_{M3}^{-} \end{pmatrix}$	$\begin{pmatrix} m_{\mathbf{Q}_1}^{z} \\ m_{\mathbf{Q}_2}^{z} \end{pmatrix}$	$\begin{pmatrix} xy, \sigma^{z} \\ xy, \sigma^{z} \end{pmatrix}$	$\begin{pmatrix} \phi_{\mathbf{Q}_1}^{(xz,yz)} \\ \phi_{\mathbf{Q}_2}^{(yz,xz)} \end{pmatrix}$	$\begin{pmatrix} xz, yz \\ yz, xz \end{pmatrix}$
$\begin{pmatrix} E_{M4}^{+} \\ E_{M4}^{-} \end{pmatrix}$	–	–	$\begin{pmatrix} \phi_{\mathbf{Q}_1}^{(xy,xy)} \\ \phi_{\mathbf{Q}_2}^{(xy,xy)} \end{pmatrix}$	$\begin{pmatrix} xy, xy \\ xy, xy \end{pmatrix}$

(iii) E_{M3}:

$$\Upsilon_{E_{M3},+}^{M} = \begin{pmatrix} 0 & \tau^{\uparrow}\sigma^{z} & 0 \\ \tau^{\uparrow}\sigma^{z} & 0 & 0 \\ 0 & 0 & 0 \end{pmatrix},$$

$$\Upsilon_{E_{M3},-}^{\Phi} = \begin{pmatrix} 0 & 0 & i\tau^{\uparrow}\sigma^{0} \\ 0 & 0 & 0 \\ -i\tau^{\uparrow}\sigma^{0} & 0 & 0 \end{pmatrix}$$

$$\Upsilon_{E_{M3},+}^{\Phi} = \begin{pmatrix} 0 & -i\tau^{-}\sigma^{0} & 0 \\ i\tau^{+}\sigma^{0} & 0 & 0 \\ 0 & 0 & 0 \end{pmatrix},$$

with

$$\tau^{\uparrow} = \begin{pmatrix} 1 & 0 \\ 0 & 0 \end{pmatrix}, \quad \tau^{\downarrow} = \begin{pmatrix} 0 & 0 \\ 0 & 1 \end{pmatrix},$$

$$\tau^{+} = \begin{pmatrix} 0 & 1 \\ 0 & 0 \end{pmatrix}, \quad \tau^{-} = \begin{pmatrix} 0 & 0 \\ 1 & 0 \end{pmatrix}$$

$$\Upsilon_{E_{M3},-}^{M} = -\begin{pmatrix} 0 & 0 & \tau^{-}\sigma^{z} \\ 0 & 0 & 0 \\ \tau^{+}\sigma^{z} & 0 & 0 \end{pmatrix},$$

acting in orbital doublet space and σ^{i} acting in spin space.

[1] D. C. Johnston, Adv. Phys. **59**, 803 (2010).
[2] J. Paglione and R. L. Greene, Nature Phys. **6**, 645 (2010).
[3] G. R. Stewart, Rev. Mod. Phys. **83**, 1589 (2011).
[4] P. Dai, J. Hu, and E. Dagotto, Nature Phys. **8**, 709 (2012).
[5] S. Avci, O. Chmaissem, J. M. Allred, S. Rosenkranz, I. Eremin, A. V. Chubukov, D. E. Bugaris, D. Y. Chung, M. G. Kanatzidis, J.-P. Castellan, J. A. Schlueter, H. Claus, D. D. Khalyavin, P. Manuel, A. Daoud-Aladine, and R. Osborn, Nature Commun. **5**, 3845 (2014).
[6] A. E. Böhmer, F. Hardy, L. Wang, T. Wolf, P. Schweiss, and C. Meingast, Nature Commun. **6**, 7911 (2015).
[7] J. M. Allred, K. M. Taddei, D. E. Bugaris, M. J. Krogstad, S. H. Lapidus, D. Y. Chung, H. Claus, M. G. Kanatzidis, D. E. Brown, J. Kang, R. M. Fernandes, I. Eremin, S. Rosenkranz, O. Chmaissem, and R. Osborn, Nature Phys. **12**, 493 (2016).
[8] W. R. Meier, Q. P. Ding, A. Kreyssig, S. L. Bud'ko, A. Sapkota, K. Kothapalli, V. Borisov, R. Valentí, C. D. Batista, P. P. Orth, R. M. Fernandes, A. I. Goldman, Y. Furukawa, A. E. Böhmer, and P. C. Canfield, npj Quantum Materials **3**, 5 (2018).
[9] R. M. Fernandes, A. V. Chubukov, and J. Schmalian, Nature Phys. **10**, 97 (2014).
[10] M. Yi, D. Lu, J.-H. Chu, J. G. Analytis, A. P. Sorini, A. F. Kemper, B. Moritz, S.-K. Mo, R. G. Moore, M. Hashimoto, W.-S. Lee, Z. Hussain, T. P. Devereaux, I. R. Fisher, and Z.-X. Shen, Proc. Natl. Acad. Sci. **108**, 6878 (2011).
[11] R. Applegate, R. R. P. Singh, C.-C. Chen, and T. P. Devereaux, Phys. Rev. B **85**, 054411 (2012).
[12] R. M. Fernandes, A. E. Böhmer, C. Meingast, and J. Schmalian, Phys. Rev. Lett. **111**, 137001 (2013).
[13] S. V. Borisenko, D. V. Evtushinsky, Z.-H. Liu, I. Morozov, R. Kappenberger, S. Wurmehl, B. Büchner, A. N. Yaresko, T. K. Kim, M. Hoesch, and N. D. Zhigadlo, Nature Phys. **12**, 311 (2015).
[14] R. M. Fernandes and O. Vafek, Phys. Rev. B **90**, 214514 (2014).
[15] V. Cvetkovic and O. Vafek, Phys. Rev. B **88**, 134510 (2013).
[16] M. H. Christensen, J. Kang, B. M. Andersen, I. Eremin, and R. M. Fernandes, Phys. Rev. B **92**, 214509 (2015).
[17] R. M. Fernandes and A. V. Chubukov, Rep. Prog. Phys. **80**, 014503 (2017).

[18] M. Tomić, H. O. Jeschke, and R. Valentí, Phys. Rev. B **90**, 195121 (2014).

[19] C.-H. Lin, T. Berlijn, L. Wang, C.-C. Lee, W.-G. Yin, and W. Ku, Phys. Rev. Lett. **107**, 257001 (2011).

[20] A. I. Coldea and M. D. Watson, Annual Rev. **9**, 125 (2018).

[21] D. Bohm, Phys. Rev. **75**, 502 (1949).

[22] E. I. Kiselev, M. S. Scheurer, P. Wölfle, and J. Schmalian, Phys. Rev. B **95**, 125122 (2017).

[23] J. Kang and Z. Tesanovic, Phys. Rev. B **83**, 020505(R) (2011).

[24] D. Podolsky, H.-Y. Kee, and Y. B. Kim, Europhys. Letts. **88**, 17004 (2009).

[25] A. V. Chubukov, R. M. Fernandes, and J. Schmalian, Phys. Rev. B **91**, 201105 (2015).

[26] A. V. Chubukov, D. V. Efremov, and I. Eremin, Phys. Rev. B **78**, 134512 (2008).

[27] C. M. Varma, Phys. Rev. B **55**, 14554 (1997).

[28] S. Chakravarty, R. B. Laughlin, D. K. Morr, and C. Nayak, Phys. Rev. B **63**, 094503 (2001).

[29] P. A. Lee and X.-G. Wen, Phys. Rev. B **78**, 144517 (2008).

[30] M. N. Gastiasoro and B. M. Andersen, Phys. Rev. B **92**, 140506 (2015).

[31] S. Graser, T. A. Maier, P. J. Hirschfeld, and D. J. Scalapino, New J. Phys. **11**, 025016 (2009).

[32] R. M. Fernandes, A. V. Chubukov, J. Knolle, I. Eremin, and J. Schmalian, Phys. Rev. B **85**, 024534 (2012).

[33] S. Lederer and S. A. Kivelson, Phys. Rev. B **85**, 155130 (2012).

[34] T. Kissikov, R. Sarkar, M. Lawson, B. T. Bush, E. I. Timmons, M. A. Tanatar, R. Prozorov, S. L. Bud'ko, P. C. Canfield, R. M. Fernandes, and N. J. Curro, Nature Commun. **9** 1058 (2018).

[35] B. G. Ueland, A. Pandey, Y. Lee, A. Sapkota, Y. Choi, D. Haskel, R. A. Rosenberg, J. C. Lang, B. N. Harmon, D. C. Johnston, A. Kreyssig, and A. I. Goldman, Phys. Rev. Lett. **114**, 217001 (2015).

[36] A. Fedorov, A. Yaresko, T. K. Kim, Y. Kushnirenko, E. Haubold, T. Wolf, M. Hoesch, A. Grüneis, B. Büchner, and S. V. Borisenko, Sci. Rep. **6**, 36834 (2016).

[37] A. V. Chubukov, M. Khodas, and R. M. Fernandes, Phys. Rev. X **6**, 041045 (2016).

[38] L. Zhao, D. H. Torchinsky, H. Chu, V. Ivanov, R. Lifshitz, R. Flint, T. Qi, G. Cao, and D. Hsieh, Nature Phys. **12**, 32 (2016).

[39] L. Fanfarillo, A. Cortijo, and B. Valenzuela, Phys. Rev. B **91**, 214515 (2015).

[40] Y. Yamakawa, S. Onari, and H. Kontani, Phys. Rev. X **6**, 021032 (2016).